Dalton Transactions

Accepted Manuscript

ROYAL SOCIETY OF CHEMISTRY

www.rsc.org/dalton

Switching-on luminescence in anilate-based molecular materials

Matteo Atzori,[†,‡] Flavia Artizzu,[†] Luciano Marchiò,*[,§] Danilo Loche,[†] Andrea Caneschi,[#] Angela Serpe,[†] Paola Deplano,[†] Narcis Avarvari,[‡] and Maria Laura Mercuri,*[,†]

[†] Dipartimento di Scienze Chimiche e Geologiche, Università degli Studi di Cagliari, S.S. 554 – Bivio per Sestu – I09042 Monserrato (Cagliari), Italy

[‡] Laboratoire MOLTECH-Anjou UMR 6200, UFR Sciences, CNRS, Université d'Angers, Bât. K, 2 Bd. Lavoisier, 49045 Angers, France

[§] Dipartimento di Chimica, Università di Parma, Parco Area delle Scienze 17A, I43124 Parma, Italy

[#] Dipartimento di Chimica "Ugo Schiff" e INSTM, Università di Firenze, Via della Lastruccia 3, I50019 Sesto Fiorentino (Firenze), Italy

TABLE OF CONTENTS GRAPHIC

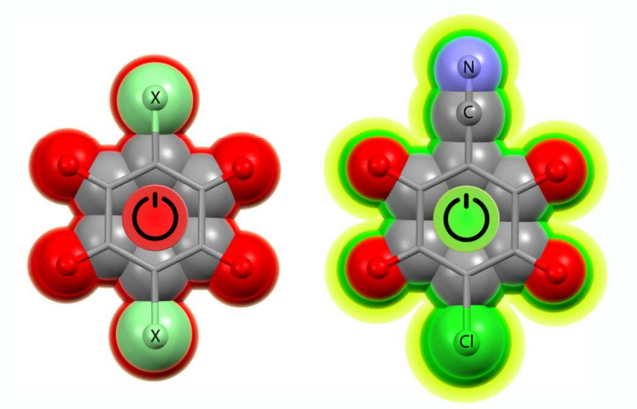

A simple substituent exchange on the chloranilate ligand induces unprecedented luminescence properties in the class of anilates and their metal complexes.

ABSTRACT: A simple change of one chloro substituent on the chloranilate ligand with a cyano group dramatically affects the electronic properties of the anilate moiety inducing unprecedented luminescence properties in the class of anilate-based ligands and their metal complexes. Here we report on the optimized synthesis and full characterization, including photoluminescence, of the chlorocyananilate ligand ($ClCNAn^{2-}$) (dianion of the 2-chloro-5-cyano-3,6-dihydroxybenzoquinone, $H_2ClCNC_6O_4$), a unique example of a heterosubstituted anilate ligand whose electronic, optical properties and coordination chemistry have never been investigated to date, even though it is known since 1966. The synthesis and full characterization of its tris-chelated metal complexes with Cr(III), Fe(III), and Al(III) metal ions are also described herein. These complexes, formulated as $[A]_3[M^{III}(ClCNAn)_3]$ (A = (n-$Bu)_4N^+$ or Ph_4P^+; M^{III} = Cr (**3**), Fe (**4**), Al (**5**)), are isostructural. While **3** and **4** are potential molecular building blocks for the preparation of molecule-based magnets or paramagnetic conducting organic-inorganic hybrid systems, **5**, instead, where the coordinated Al(III) metal ions retains the luminescence of the ligand, represents a unique building block to achieve heterobimetallic assemblies showing emissive properties under visible light irradiation.

INTRODUCTION

One of the current major challenges in molecular nanoscience is the synthesis of new molecule-based materials exhibiting more than one physical property within the same crystal lattice. Of significant importance is the combination of magnetic properties with one or more additional properties, such as conductivity,[1] chirality[2] and luminescence.[3] This is due to the fact that such multifunctional molecular materials can find potential applications in the fields of molecular electronics, spintronics and photonics.[4] Molecular electronics is an emerging area of research based on the construction and fabrication of molecular species showing peculiar magnetic properties, stability and robustness, which primarily require to retain their structures and properties in solution in order to undergo processing procedures such as deposition on electrical conducting surfaces.[5]

In this context, crystal engineering, the art of designing synthetic crystalline materials through the knowledge of the electronic, steric, topological and intermolecular interactions between the functional groups of their constituent building blocks,[6-9] offers a powerful tool for combining different physical properties in these systems. One of the most powerful strategies to design such materials is based on the use of tectons,[6-9] in particular metallotectons which are metal complexes able to be involved in well identified intermolecular interactions. There are several advantages of employing metallotectons to construct supramolecular architectures or coordination polymers. In particular it is possible to tune both the coordination geometry around the metal centre, the bonding capability at the complex's periphery, and the metallotecton shape, by varying the metal, its oxidation state, and/or the organic ligands used. It therefore becomes apparent that one of the most important factors for the construction of new materials with dual physical properties is the choice of the organic chelating ligand. This often dictates not only the molecular topology, but also the nature of the intramolecular magnetic exchange interactions and the efficiency of the light harvesting/emission properties or the capability of working as a sensitizer ('antenna') toward an external luminophore, which can be connected through covalent or non-covalent bonding.

A family of such multi-acting organic ligands is represented by the anilates,[10] namely dianions of 3,6-disubstituted-2,5-dihydroxy-1,4-benzoquinones, which have been increasingly used as suitable ligands for the preparation of functional molecular building blocks able to be employed for the construction of supramolecular architectures,[11-13] coordination polymers[14-17] or as paramagnetic components of hybrid organic-inorganic systems[18] with peculiar physical properties. The special interest devoted to this class of ligands is related to *(i)* the ability to

coordinate metal ions in various coordination modes,[10] *(ii)* the ability to further coordinate a second metal ion due to the presence of two peripheral coordinating C–O groups,[10,14-17] *(iii)* non-innocent redox properties and easy reduction process to a radical-anion form.[10,19,20] Moreover, anilate ligands can be easily functionalized by introducing suitable substituents on the 3 and 6 positions which are capable of *i)* modulating the magnetic exchange interactions between coordinated metal ions,[14,21] *ii)* giving rise to various supramolecular interactions which affect the dimensionality and the physical properties of the final system,[11-13,22] and *iii)* promoting intramolecular charge-transfer (CT) towards the electron-poor benzoquinone moiety,[23] without affecting the coordinating properties.

The possibility to introduce additional properties to the ligand and the corresponding metal complexes by functionalizing the anilate moiety through specific substituent groups, recently attracted our attention, and, in particular, the introduction of luminescent properties in the class of anilate-based materials was envisaged to afford multifunctional materials with potential combination or interplay between magnetism and luminescence.

Since the presence of cyano substituents directly connected to the benzoquinone moiety in its reduced form (1,4-dihydroxybenzene) are known to induce luminescent properties,[24] the heterosubstituted chlorocyananilate ($ClCNAn^{2-}$) (dianion of the 2-chloro-5-cyano-3,6-dihydroxybenzoquinone, $H_2ClCNC_6O_4$) has been selected as potential luminophore to introduce a new physical property in this class of ligands without altering their structural/electronic features.

The chlorocyananilate ligand was briefly described in 1966,[25] but, surprisingly, to the best of our knowledge no metal complexes with this ligand have been reported, although its reactivity towards metal ion coordination is expected to be very similar with respect to the homosubstituted chloranilate.[10]

To further explore the chemistry of anilate-based complexes and to enlarge the range of functionalities achievable in this class of compounds, we report herein the optimized synthesis of the $ClCNAn^{2-}$ ligand and its tris-chelated metal complexes with Cr(III), Fe(III), and Al(III), namely $[Cr(ClCNAn)_3]^{3-}$ (**3**), $[Fe(ClCNAn)_3]^{3-}$ (**4**), $[Al(ClCNAn)_3]^{3-}$ (**5**), with their full characterization including analytical and structural data, spectroscopic and physical studies, also supported by theoretical calculations at the DFT and TD-DFT level. The magnetic properties of **3** and **4**, which represent valuable molecular bricks for the preparation of molecule-based magnets or paramagnetic conducting organic-inorganic hybrid systems are described, along with the investigation of the optical properties of the ligand in its

monoprotonated (**1**) and dianionic (**2**) form, and its Al(III) complex (**5**), which represent a potential building block to afford luminescent heterobimetallic assemblies.

RESULTS AND DISCUSSION

Synthesis. Chlorocyananilic acid can be obtained by treating 2,3-dicyano-5,6-dichloro-1,4-benzoquinone with a concentrated water solution of potassium hydroxide, followed by acidification with concentrated hydrochloric acid (Scheme 1).

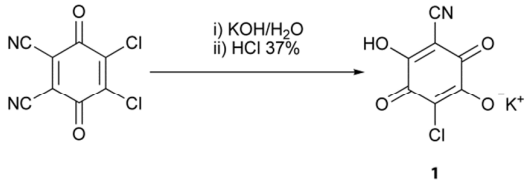

1

Scheme 1. Synthesis of the monoprotonated form of chlorocyananilic acid.

This method provides in good yield $ClCNAn^{2-}$ in its monoprotonated form HKClCNAn (**1**) as orange crystalline solid. All attempts to isolate and crystallize the bis-protonated chlorocyananilic acid ($H_2ClCNAn$) were unsuccessful. This is not surprising given the strong acidity of this ligand due to the presence of the cyano group (pK_a value for $H_2(CN)_2An$ = –0.5)[26] which favors the anionic forms.

In order to get deeper insight on the molecular structure of this ligand, the chlorocyananilate dianion as $[Ph_4P]^+$ salt, $[Ph_4P]_2[ClCNAn]\cdot 2H_2O$ (**2**), has been prepared and its crystal structure determined. Compound **2** was obtained by recrystallizing **1** in a basic aqueous solution containing Ph_4PBr.

The tris(chlorocyananilato)metallate(III) complexes **3**-**5** (see Chart 1) were prepared according to the general synthetic strategy recently reported for obtaining the family of the analogous tris(haloanilato)metallate(III) complexes,[22] as illustrated in Scheme 2.

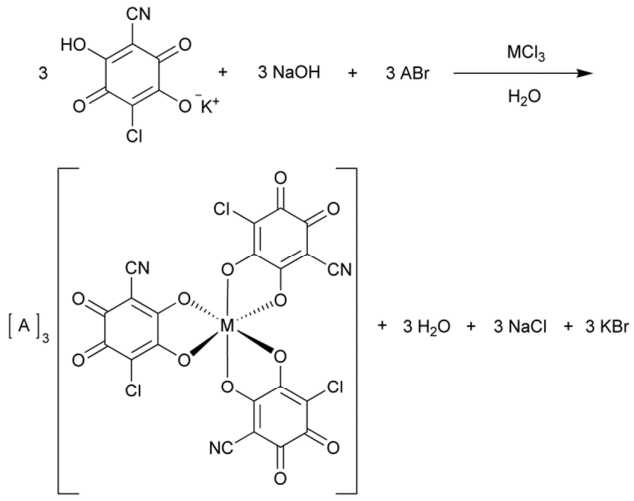

Scheme 2. General reaction scheme for the synthesis of the $[A]_3[M(ClCNAn)_3]$ (A = $(n\text{-}Bu)_4N^+$ or Ph_4P^+; M = Cr(III), Fe(III), Al(III)) complexes.

These complexes were obtained in high yields (75–95%) through a one-pot reaction between the trivalent metal ion (M = Cr(III), Fe(III), or Al(III)) and the chlorocyananilate dianion obtained *in situ* in an aqueous solution.

Chart 1.

	$ClCNAn^{2-}$		
	Cr(III)	Fe(III)	Al(III)
$[(n\text{-}Bu)_4N]^+$	**3a**	**4a**	**5a**
$[Ph_4P]^+$	**3b**	**4b**	**5b**

Crystal structures. Single crystals of compound **1** were obtained by recrystallization of the crude product in an acid hydrochloric water solution. Compound **1** crystallizes in the monoclinic $P2_1/a$ space group with one independent $HClCNAn^-$ molecule in the unit cell and a potassium cation. An ORTEP drawing for **1** with atoms labeling scheme is reported in Figure 1a.

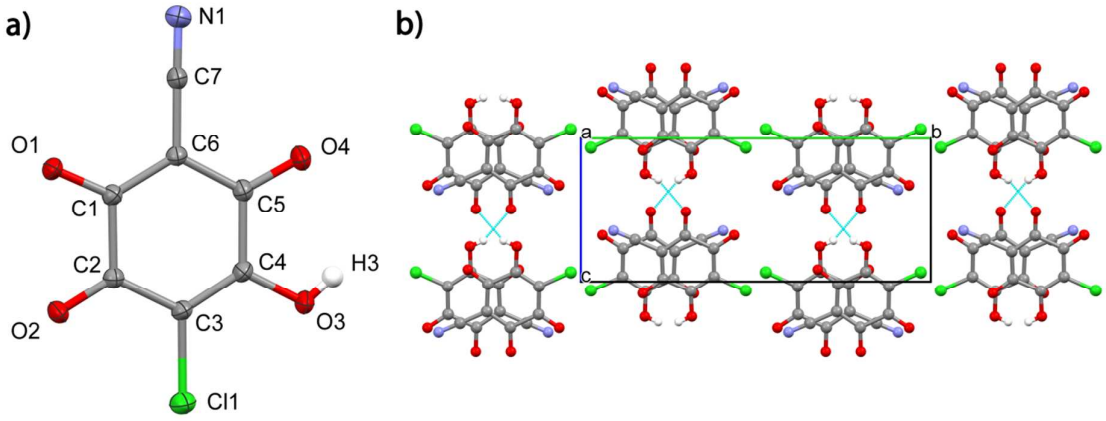

Figure 1. a) ORTEP drawing of **1** with thermal ellipsoids at 30% probability level. Selected bond distances: C(1)–O(1) 1.247 Å, C(2)–O(2) 1.215 Å, C(5)–O(4) 1.234 Å, C(4)–O(3) 1.326 Å. b) View of the crystal structure of **1** where the stacked columns of $HClCNAn^-$ along the *a* crystallographic axis are highlighted. Potassium cations are omitted for clarity.

The molecular structure of the benzoquinone ring shows intermediate features with respect to the centrosymmetric quinoidal form typical of the bis-protonated anilic acids[27-31] and the non quinoidal form of the dianions.[32-37] In fact, it presents three C–O bonds, in the 1.215–1.247 Å distance range, slightly longer than pure C=O bonds, whereas one C–O distance of 1.326 Å is typical of single C–O bonds and it is associated to the protonated oxygen. Moreover, the four C–C distances associated to the O–C–C(–X)–C–O bonds fall in the shorter 1.344–1.454 Å range than the two other C–C bonds (C(1)–C(2) and C(4)–C(5)) which are slightly longer (1.548 Å and 1.507Å). The C(6)–C(7) and C(7)–N(1) bond distances, of 1.434 Å and 1.146 Å, respectively, are typical of pure single C–C and triple C–N bonds, indicating that the cyano substituent is not conjugated with the C(1)–C(6)–C(5) allylic fragment of the ring.

The crystal structure of **1** shows parallel columns of monoprotonated acid stacked along the *a* crystallographic axis which interact through hydrogen-bonds exchanged between the O(3)–H(3) donor and the O(1) acceptor (O(3)···O(1) distance 2.709 Å) (Figure 1b). The columns are separated by potassium cations exhibiting a nona-coordinated tri-capped trigonal prism coordination geometry (Figure 2a) by four O atoms, two Cl atoms and two N atoms of the monoprotonated chlorocyananilate (Figure 2b).

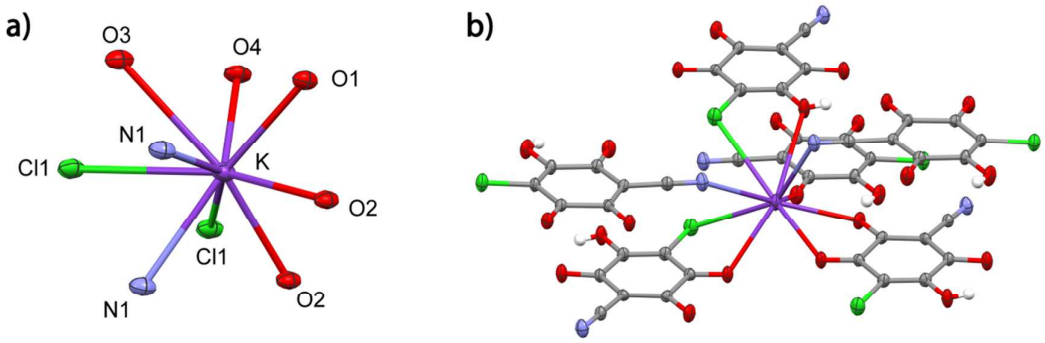

Figure 2. Coordination environment around the potassium cations for **1** where a) the tri-capped trigonal prism geometry and b) the coordinating molecules are highlighted.

Both the $K^{+}\cdots O$ and $K^{+}\cdots Cl$ distances, ranging from 2.722 to 3.311 Å, and from 3.369 to 3.449 Å, respectively, and the coordination environment exhibited by the potassium cations, are similar to those already observed for the analogous compound $KHCl_2An\cdot 2H_2O$.[37]

Compound **2** crystallizes in the triclinic centrosymmetric space group *P–1* with one half $ClCNAn^{2-}$ molecule, one $[Ph_4P]^{+}$ cation and one water molecule as independent units in the unit cell. The chloro and cyano substituents on the $ClCNAn^{2-}$ anion were found disordered in two equivalent positions (0.50 and 0.50 site occupancy factors) related to two possible orientations of the ligand along an ideal plane formed by the planar benzoquinone ring.

The molecular structure of **2** shows the typical features of the anilate dianions[32-37] *i)* a planar structure of the benzoquinone moiety, *ii)* four C–O bonds of similar length (1.232–1.243 Å), *iii)* four C–C bonds of similar length (1.414–1.424 Å), and *iv)* two C–C bonds considerably longer (1.542 Å).

The crystal structure of **2** consists of chlorocyananilate anions connected through a hydrogen-bond in supramolecular chains. This hydrogen-bond involves the O1w water molecule and the O(2) and N(1) (or Cl(1)) atoms of two adjacent ligands (Figure 3a). No interactions between the chains were observed being separated by the bulky $[Ph_4P]^{+}$ cations (Figure 3b).

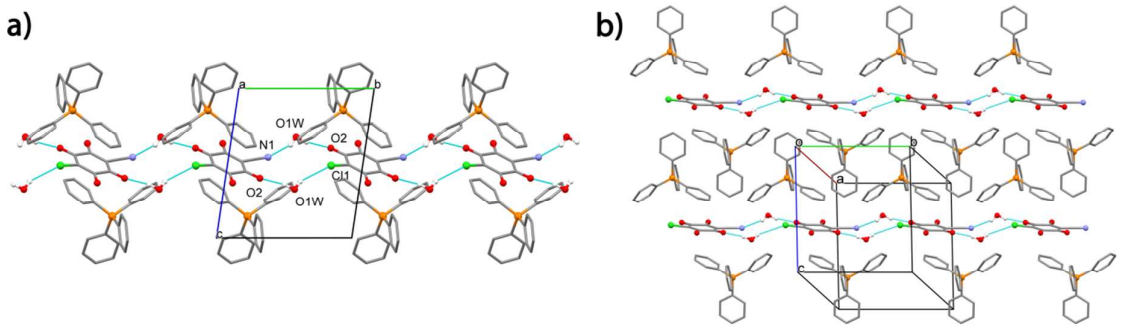

Figure 3. View of the crystal structure of **2**. a) $ClCNAn^{2-}$ anions connected in supramolecular chains through hydrogen-bonding interactions along the *b* crystallographic axis, b) two chains separated by $[Ph_4P]^+$ cations. Selected bond distances and angles: N(1)···O(1w) 2.991 Å, O(1w)···O(2) 2.870 Å, O1w–H1A···O(2) 2.013 Å, O(1w)–H(2A)···O(2) 166.51°.

The crystal structures of the M(III) chlorocyananilate complexes consist of homoleptic tris-chelated complex anions of formula $[M(ClCNAn)_3]^{3-}$ (M = Cr(III), Fe(III), Al(III)) and $[(n\text{-}Bu)_4N]^+$ or $[Ph_4P]^+$ cations. These complexes exhibit octahedral geometry with the metal bound by six oxygen atoms from three chelating ligands. According to the metal coordination of three bidentate ligands, the metal complexes are chiral, but in the crystal lattice both Λ and Δ enantiomers are present as evidenced by the centrosymmetry of all the space groups. The molecular structure of the complex anion for **3a** is reported in Figure 4 whereas that of **4a** is reported in Figure S1 in the Supporting Information.

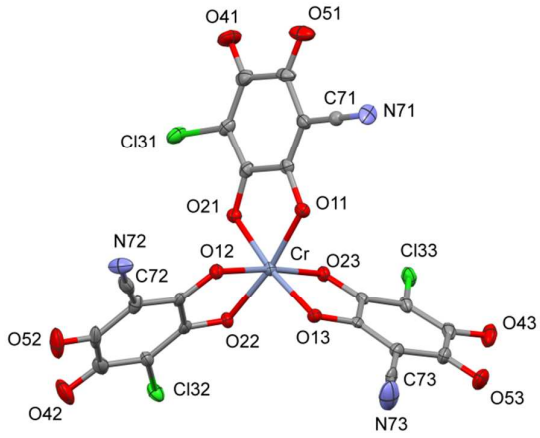

Figure 4. ORTEP drawing for the anionic complex (Λ enantiomer) for **3a** with thermal ellipsoids at the 30% probability level along with principal atoms labelling scheme.

The metal-oxygen bond distances range from 1.965(4)–1.986(4) Å and 1.997(3)–2.023(3) Å for the Cr(III) and Fe(III) complexes, respectively, and are in agreement with the high spin character of these systems (*vide infra*) (Table 1).

Table 1. M–O bond distances (Å) for the anionic complex of compounds **3a**, **3b** and **4a**.

Bonds	**3a**	**3b**	**4a**
M–O(11)	1.965(4)	1.966(3)	1.997(3)
M–O(21)	1.969(4)	1.968(3)	2.019(3)
M–O(12)	1.975(4)	1.968(3)	2.008(3)
M–O(22)	1.977(3)	1.977(3)	2.017(3)
M–O(13)	1.976(3)	1.982(3)	2.023(3)
M–O(23)	1.978(3)	1.973(3)	2.018(3)
Average M–O	1.973(4)	1.972(3)	2.014(3)

The C–O bond distances are influenced by the metal coordination as evidenced by the fact that the oxygen atoms bound to the metal lead to C–O distances that are, on average, 0.06 Å longer than those involving the peripheral uncoordinated oxygen atoms (Table 2).

Table 2. C–O bond distances (Å) for the anionic complex of compounds **3a**, **3b** and **4a**.

Bonds	**3a**	**3b**	**4a**
C(11)–O(11)	1.292(6)	1.275(7)	1.283(5)
C(21)–O(21)	1.292(6)	1.215(6)	1.282(5)
C(41)–O(41)	1.222(7)	1.229(8)	1.226(5)
C(51)–O(51)	1.230(7)	1.204(9)	1.227(5)
C(12)–O(12)	1.286(6)	1.287(4)	1.292(5)
C(22)–O(22)	1.279(7)	1.286(4)	1.282(5)
C(42)–O(42)	1.233(7)	1.233(5)	1.237(5)
C(52)–O(52)	1.223(7)	1.222(5)	1.228(5)
C(13)–O(13)	1.296(7)	1.290(4)	1.278(5)
C(23)–O(23)	1.287(7)	1.280(4)	1.282(5)
C(43)–O(43)	1.232(7)	1.229(5)	1.217(5)
C(53)–O(53)	1.228(7)	1.222(5)	1.224(5)

The bond distances of the peripheral C–O moieties are, thus, in agreement with a double bond character. Accordingly, the chlorocyananilate ligand presents the typical *o*-quinone-like resonance structure upon metal coordination.[10]

Compounds **3a** and **4a** are isostructural, therefore their crystal structures can be described together. These compounds crystallize in the monoclinic $P2_1/a$ space group with one $[M(ClCNAn)_3]^{3-}$ (M = Cr(III), Fe(III)) complex anion and three $[(n\text{-}Bu)_4N]^+$ cations in the asymmetric unit. Their crystal packing is characterized by the presence of C–N···Cl interactions between complex anions having opposite stereochemical configuration (Λ, Δ), responsible for the formation of infinite 1D supramolecular chains parallel to the *a* crystallographic axis (Figure 5). The C–N···Cl interactions are characterized by a Cl···N distance of 3.064 and 3.121 Å, for **3a** and **4a**, respectively, that are shorter than the sum of chlorine and nitrogen van der Waals radii (3.30 Å), and a C–Cl···N angle of ca. 155.0° and 153.5°, for **3a** and **4a**, respectively. Therefore, the Cl···N interaction can be regarded as a halogen-bond where the chlorine behaves as halogen-bonding donor and the nitrogen atom as the halogen-bonding acceptor. This is in agreement with the properties of the electrostatic potential for the $[M(ClCNAn)_3]^{3-}$(M = Cr(III), Fe(III)) anions that predicts a negative charge accumulation on the nitrogen atom of the cyano group and a positive charge accumulation on the chlorine (*vide infra*). No close contacts between the chains were observed since they are well separated by the presence of $[(n\text{-}Bu)_4N]^+$ cations (omitted for clarity in Figure 5).

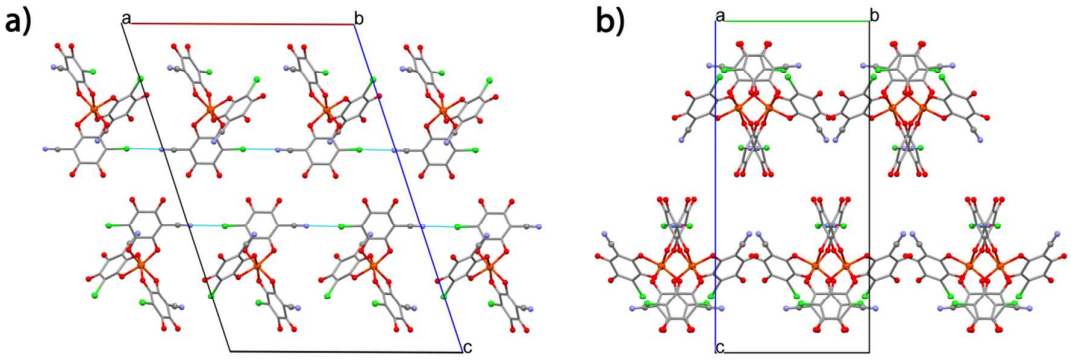

Figure 5. a) Portion of the molecular packing of **4a** showing the Cl···N interactions occurring between the complex anions; b) View of the supramolecular chains along the *a* axis. $[(n\text{-}Bu)_4N]^+$ cations are omitted for clarity.

Powder X-ray diffraction (PXRD) measurements performed on a polycrystalline sample of **5a**, *i.e.* the $[(n\text{-Bu})_4N)]_3[Al(ClCNAn)_3]$ Al(III) complex, show that this compound is isostructural with its Cr(III) and Fe(III) analogues (Supporting Information, Figure S2).

Compound **3b** crystallizes in the monoclinic $P2_1/n$ space group with one $[Cr(ClCNAn)_3]^{3-}$ complex anion, three $[Ph_4P]^+$ cations and one water molecule in the asymmetric unit. This compound is isostructural with respect to the already reported analogous system having chloranilate as ligand.[22] The presence of $[Ph_4P]^+$ cations in the crystal structure is responsible for the formation of π–π interactions between the aromatic rings of the cations and the quinoid ring of the three anilate ligands. In fact, the complex anions are surrounded by several $[Ph_4P]^+$ cations exchanging π–π interactions through their phenyl rings with each chlorocyananilate ligand (Figure 6).

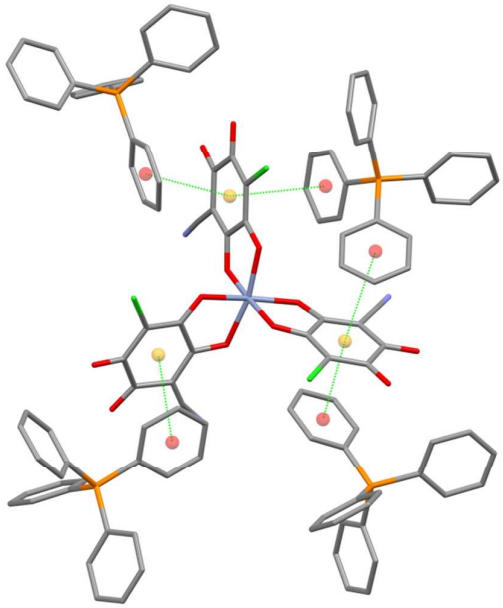

Figure 6. Portion of the crystal structure of **3b** where the π–π interactions occurring between the complex anions and the $[Ph_4P]^+$ cations are highlighted. The ligand–phenyl centroids distances are in the 3.531–4.073 Å range. The shortest C···C contacts are in the 3.289–3.372 Å range" The crystallization water molecule and $[Ph_4P]^+$ molecules not directly involved in the π–π interactions are omitted for clarity.

These interactions preclude a close contact between the complex anions whose shortest intermolecular M···M distances are of ca. 13.50 Å.

PXRD measurements performed on polycrystalline samples of **4b** and **5b**, *i.e.* the Fe(III) and Al(III) complexes having $[Ph_4P]^+$ as counterion, evidenced that these compounds are isostructural with the above described Cr(III) analogue **3b** (Supporting Information,

Figure S3). Therefore, the crystal packing of **4b** and **5b** can be considered the same as **3b** except for small deviations on the bond distances related to the coordination to a different metal centre.

DFT Calculations. DFT calculations were performed to gain insight into the charge distribution of the $ClCNAn^{2-}$ ligand and the $[M(ClCNAn)_3]^{3-}$ (M = Cr(III) (**3**), Fe(III) (**4**), Al(III) (**5**)) complexes. Since the coordination environment comprises six oxygen donor atoms, and according to the geometric parameters obtained by the crystal structures and the magnetic data (*vide infra*), the calculations were performed in the high spin state for the Cr(III) (S = 3/2) and Fe(III) (S = 5/2) complexes. As previously reported for similar complexes,[11,22] Mulliken and natural population analysis (NPA) schemes were employed in order to provide a more complete description of the atomic charges in the six anionic complexes.[38] In both isolated ligand and complexes, the negative charge is mainly localized on the four oxygen atoms and on the nitrogen atom of the cyano group (Figure 7).

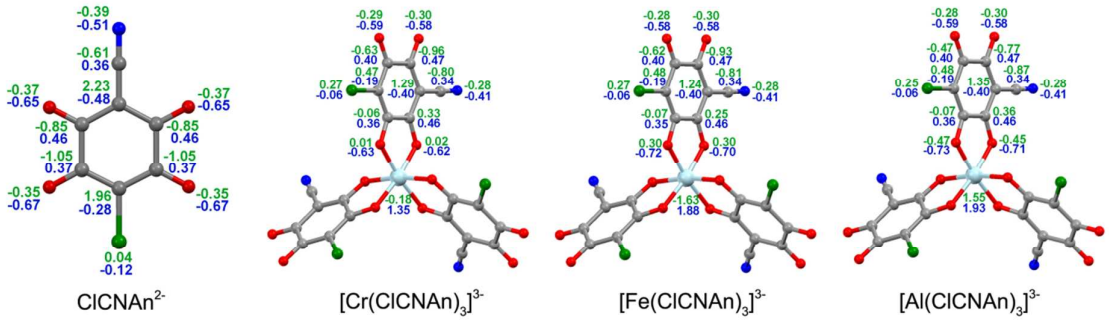

Figure 7. Mulliken (green) and NPA (blue) charges for $ClCNAn^{2-}$ (B3LYP/6-311+G(d)), and for $[Cr(ClCNAn)_3]^{3-}$, $[Fe(ClCNAn)_3]^{3-}$, and $[Al(ClCNAn)_3]^{3-}$ (B3LYP/6-311+G(d)-lanl2tz). The charges of only one ligand are depicted for clarity.

When comparing the charge profile of the heterosubstituents, Cl and CN, it is evident that the nitrogen present a higher negative charge accumulation than the chlorine. According to the NPA scheme, the chlorine atom bears a negligible negative charge, whereas according to the Mulliken scheme the charge is even positive. Moreover, within the hexaatomic ring, the NPA analysis shows that the carbon atoms linked to the oxygens bear positive charges, whereas the carbon atoms linked to the Cl and CN groups have negative charges (Figure 7).

The charge distribution obtained by analysing the atomic charges is also substantiated by the electrostatic potential (EP) of the ligand and the three metal complexes (Figure 8 and Figure S7).

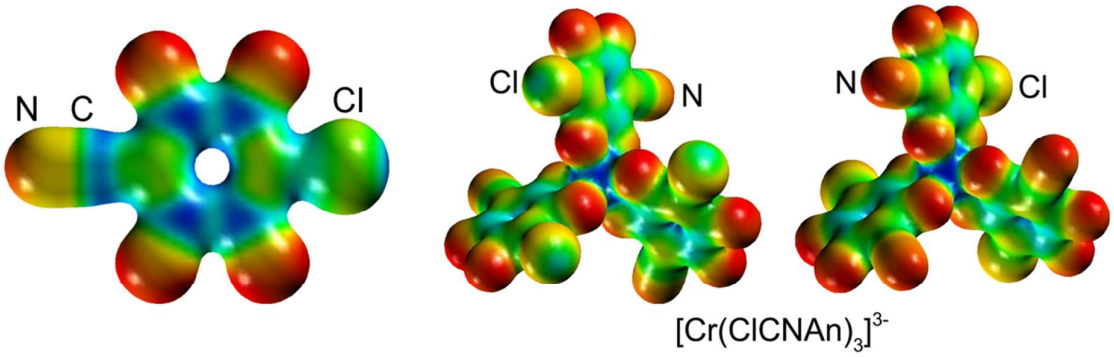

Figure 8. Electrostatic potential for $ClCNAn^{2-}$ (B3LYP/6-311+G(d)) and $[Cr(ClCNAn)_3]^{3-}$ mapped on the isodenisty surface. Color codes thresholds: red –0.3, yellow –0.2, green –0.15, light blue –0.1, blue 0.0. A comparison of the electrostatic potential for the three metal complexes are reported in Figure S7 in the Supporting Information.

The isodensity surface mapped with the electrostatic potential shows for all systems that the oxygen atoms are the source of greater negative charge accumulation followed by the nitrogen atom of the CN moiety. Moreover, there is a moderate negative charge accumulation on the carbon atoms linked to the Cl and CN groups, whereas the remaining four carbon atoms, which are linked to the oxygen atoms, exhibit a positive charge. The chlorine atom present a typical positive charge on the opposite side of the C–Cl vector and a ring of negative charge perpendicular to the same vector, in line with the σ-hole model of the electron density distribution[39]. The overall charge distribution for the complexes implies that the coordinated ligand may act simultaneously as a halogen-bond donor (through the Cl substituent) and acceptor (through the CN substituent and the peripheral oxygen atoms).

As for strictly related systems,[11,22] when comparing the two paramagnetic complexes, the Cr(III) complex exhibits a more localized spin distribution on the metal center than the Fe(III) complex (Figure S8). According to the NPA scheme, the spin density is 2.96 on the Cr(III) and 4.26 on Fe(III) centers, respectively (Table 3).

Table 3. Mulliken and NPA charges and spin densities on metal centers together with the expectation values of the $<S^2>$ operator for $[Cr(ClCNAn)_3]^{3-}$, $[Fe(ClCNAn)_3]^{3-}$, and $[Al(ClCNAn)_3]^{3-}$.

	Mulliken spin density	Mulliken charges	NPA spin density	NPA charges	$<S^2>^a$
$[Cr(ClCNAn)_3]^{3-}$	2.960	–0.178	2.835	1.351	3.771 (3.750)
$[Fe(ClCNAn)_3]^{3-}$	4.263	–1.630	4.116	1.879	8.760 (8.750)
$[Al(ClCNAn)_3]^{3-}$	-	1.551	-	1.928	-

[a] = in parenthesis, after annihilation of the first spin contaminant

Consistently, in the Fe(III) complex the shape of the total spin density is markedly distributed over the six oxygen atom of the coordination sphere (Figure S8).

Vibrational Spectroscopy. In the 3100–2900 cm^{-1} region of the FT-IR spectra of **3a**, **4a** and **5a**, the typical ν(C–H) vibrational modes of the $[(n\text{-}Bu)_4N]^+$ counterion are present. The ν(C–N) vibrational mode related to the CN substituent of the chlorocyananilate ligand is present as a sharp band centered at 2213 cm^{-1}. A comparison between the spectra of **3a**, **4a**, and **5a** in the 1750–700 cm^{-1} region is provided in Figure S9. The presence of the same vibrational bands, with similar shape and relative intensity, further confirms the same chemical environment, and therefore the same coordination geometry, for the $[M(ClCNAn)_3]^{3-}$ (M = Cr(III), Fe(III), Al(III)) complexes, in agreement with single crystal and powder XRD results.

The band centered at ca. 1650 cm^{-1} is assigned to the ν(C=O) vibration mode for the uncoordinated C=O groups of the ligand.[40] A downshift of this band respect to the free ligand (1676 cm^{-1}) is observed and it can be attributed to a weakened double bond character of the terminal C=O groups due to the coordination with the metal ion, in agreement with the structural findings. The weak band present at 1612 cm^{-1}, not present in the FT-IR spectra of their chloranilate analogues,[22] may be related to a combination band involving CN vibrational modes. The strong and broad bands centered at ca. 1560 cm^{-1} and 1530 cm^{-1} for **3a** and **4a**, slightly shifted to 1580 cm^{-1} and 1550 cm^{-1} for **5a**, can be assigned to ν(C=C) + ν(C=O) combination bands.[40] The band present at 1395 cm^{-1} for **3a** and **4a**, and at 1340 cm^{-1} for **5a**, is assigned to the ν(C–C) + ν(C–O) combination band, whereas the one at ca. 1310 cm^{-1} is assigned to the ν(C–C) vibration.[40] Compounds **3a**, **4a** and **5a** show two additional bands at ca. 1325 cm^{-1} and 1260 cm^{-1} with respect their chloranilate analogues,[22] whose origin may be related to vibrational modes involving the cyano group. The two bands centered at ca. 1030 cm^{-1} and ca. 860 cm^{-1} can be related to the ν(C–C) + ν(C–O) + δ(C–Cl), and to the δ(C=O) + δ(C–O) + ν(C–Cl), combination bands, respectively.[40] Interestingly, an upward shift of these bands is observed when compared to the same bands of their chloranilate analogues (ca. 995 cm^{-1} and 840 cm^{-1}, respectively).[22] It is noteworthy that in the 700–400 cm^{-1} region the spectra of the three metal complexes show some differences. Except for the wagging vibrational mode related to the C–Cl bond centered at ca. 610 cm^{-1} for all compounds,[40] three bands at ca. 580, 510, 420 cm^{-1} are present for **4a**, and four bands at 625, 596, 517, 444 cm^{-1} and at 636, 598, 489, 450 cm^{-1} are present for **3a** and **5a**, respectively. These bands, that are

not present in the ligand and counterion spectra, can be related to vibrational modes involving M–O bonds (Figure S10).

The FT-IR spectra of compounds **3b**, **4b** and **5b** show the same features except for the contributions of the different counterion.

UV-Vis Spectroscopy and TD-DFT Calculations. The UV-Vis absorption spectra of **1** and **2** show similar features in the 230–800 nm region (Figure 9). The absorption spectrum of **2**, recorded in CH_3CN for solubility reasons, shows two intense bands in the UV region centered at λ_{max} = 268 nm and 318 nm, with extinction coefficients of ε = 19718 dm^3 mol^{-1} cm^{-1} and 23262 dm^3 mol^{-1} cm^{-1}, respectively, and one band in the Vis region centered at λ_{max} = 460 nm, with an extinction coefficient two orders of magnitude smaller (ε = 526 dm^3 mol^{-1} cm^{-1}). The same features are observed in the UV-Vis absorption spectra of **1** in H_2O, in its protonated or dianionic form (red and blue lines in Figure 9, respectively) obtained *in situ* by adding an excess of concentrated HCl or Et_3N to the corresponding solutions, to avoid possible protic equilibria. These bands are observed at λ_{max} = 251 nm (ε = 10405 dm^3 mol^{-1} cm^{-1}), 305 nm (ε = 16036 dm^3 mol^{-1} cm^{-1}), and 464 nm (ε = 512 dm^3 mol^{-1} cm^{-1}), and at λ_{max} = 261 nm (ε = 13361 dm^3 mol^{-1} cm^{-1}), 316 nm (ε = 19973 dm^3 mol^{-1} cm^{-1}), and 487 nm (ε = 438 dm^3 mol^{-1} cm^{-1}), for the protonated and dianionic forms, respectively (Figure 9). The UV-Vis spectrum of **1** in its dianionic form is red-shifted when compared to that of its protonated form. This is very likely due to the energy stabilization of the dianion in water. Moreover, while the two high-energy bands of **1** under basic conditions, closely resemble those of the dianionic ligand form of **2**, only the low-energy band in the visible region is clearly affected by solvent polarity, as it is significantly red-shifted in H_2O solution (blue line) with respect to CH_3CN (orange line).

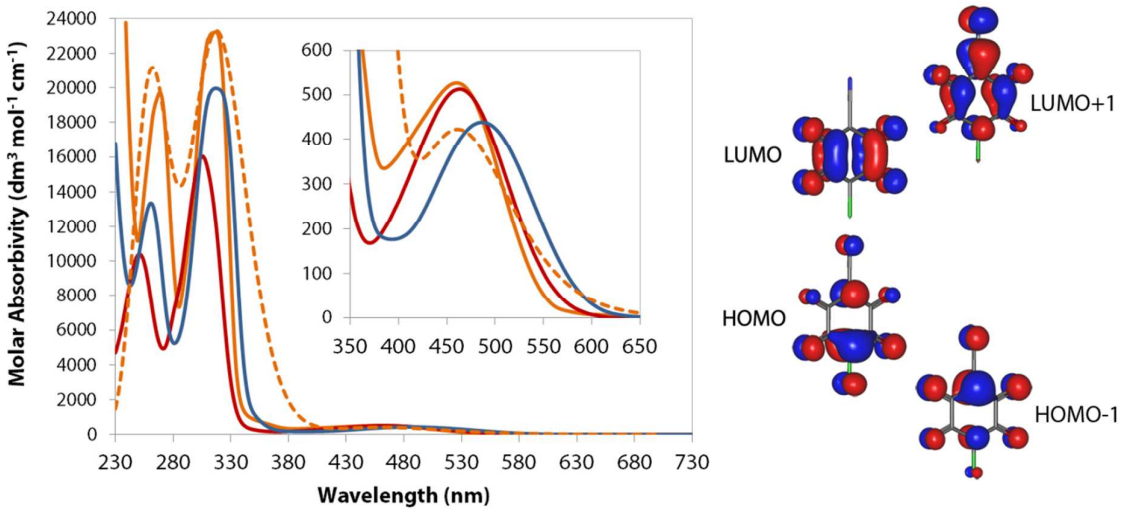

Figure 9. (left) Experimental UV-Vis spectra (230–730 nm) for **2** in CH_3CN solution (orange line), and **1** in H_2O solution in its protonated (red line) and dianionic (blue line) forms, along with the calculated spectrum for **2** in CH_3CN solution (orange dashed line). Inset shows the Vis region. (right) Spatial plots of frontiers molecular orbitals of $ClCNAn^{2-}$ (B3LYP/6-311+G(d) PCM(CH_3CN), isovalue = 0.04).

In the diffuse reflectance (DR) spectra recorded on polycrystalline samples of **1** and **2** in the 350–750 nm Vis region, the same absorption band observed in solution at ca. λ_{max} = 460 and 490 nm, for **1** and **2**, respectively, appears red-shifted and broadened as result of solid state effects (Figure S11).

DFT and TD-DFT calculations were performed in order to rationalize the electronic spectra of the chlorocyananilate ligand and its metal complexes. In Figure 9 the calculated UV-Vis spectrum of **2** in CH_3CN using the polarizable continuum model (PCM) method is reported. An excellent agreement between the calculated UV-Vis profile and the experimental one is observed. In order to explain the type of transitions occurring for **2** in CH_3CN, it is appropriate to briefly describe the shape of the frontier molecular orbitals (MOs) of **2** (Figure 9). The most intense transitions (those with the greater oscillator strength, *f*, see Table S1) mainly involve four orbitals, namely HOMO-1, HOMO, LUMO and LUMO+1. These molecular orbitals are all of π-type. In particular, HOMO-1 is an antibonding orbital involving the nitrogen and oxygen atoms and the carbon atom of the C–CN group. An approximately opposite shape is exhibited by the HOMO, which is partly localized on the C–Cl moiety. The LUMO is an antibonding orbital with respect to the C–O fragments and it is localized on the two O–C–C–O systems, whereas a good portion of the LUMO+1 involves the CN group. The transition in the Vis region (λ_{max} = 463 nm) is characterized by a low intensity and it is mainly associated to a HOMO → LUMO transition (Table S1). The most intense bands occur at λ_{max}

= 318 nm and 261 nm and are associated to the HOMO-1 → LUMO and HOMO → LUMO+1 transitions, respectively. These considerations suggest that the observed transitions are dependent on the different functionalization of the anilate moiety, with the chlorine atom and cyano group affecting the shape of the frontiers MOs.

It is useful to compare the electronic properties of the symmetric homosubstituted Cl_2An^{2-} ligand with those of **2** (Figure S12). The shapes of the frontier molecular orbitals (HOMO and LUMO) are very similar, but in **2** the presence of two different functionalizations on the quinoid ring, namely the Cl and CN substituents, leads to a symmetry breaking. Consequently, the HOMO in **2** is not centrosymmetric whereas the LUMO maintains the center of symmetry. This makes the HOMO → LUMO transition, and the corresponding absorption band in the Vis region (computed at 463 nm), partly allowed in **2**. On the opposite, in Cl_2An^{2-} both the HOMO and LUMO are centrosymmetric and the band in the Vis region is predicted to have a null intensity (Figure S12 and Table S2). This is confirmed by the experimental absorption spectrum of Cl_2An^{2-} where the intensity of the visible band is considerably lower than **2**.

The UV-Vis absorption spectra of **3a**, **4a** and **5a** metal complexes are reported in Figure 10.

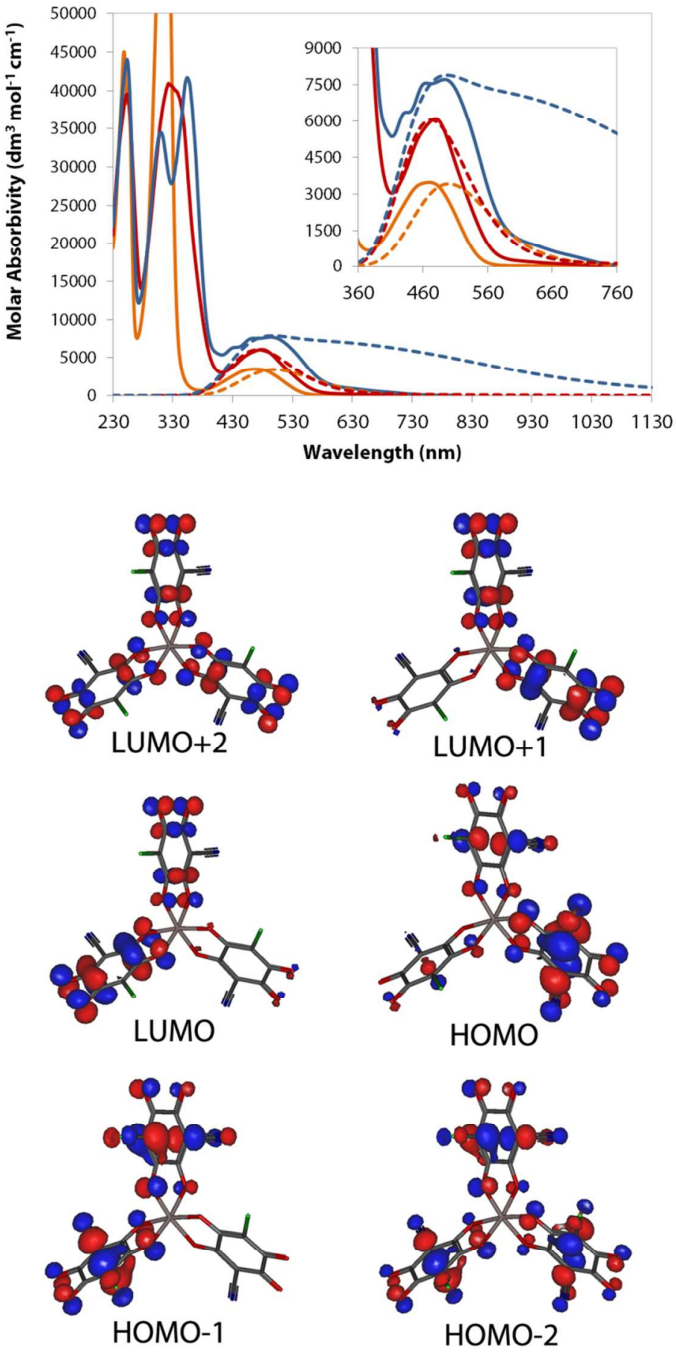

Figure 10. (above) Experimental (solid lines) and calculated (dashed lines) UV-Vis spectra (230–730 nm) for **3a** (red line), **4a** (blue line), and **5a** (orange line) in CH_3CN solution. Inset shows the Vis region. (below) Spatial plots of the frontiers molecular orbitals of $[Al(ClCNAn)_3]^{3-}$ computed by TD-DFT/PCM(CH_3CN) B3LYP/3-21+G, isovalue = 0.04).

Overall, the spectra of the complexes show similar features with respect to the free ligand, with two intense absorption bands in the 200–400 nm region, and a less intense absorption in the 360–760 nm Vis region. These bands are slightly red-shifted with respect to that of the

free ligand as a consequence of ligand stabilization due to coordination, and this effect is more pronounced in the case of **3a** and **4a** metal-*d* complexes according to the more covalent character of the bond compared to the **5a** Al(III) complex. For all complexes, the lowest absorption band appears to be resolved into multiple bands, and this fine structure is more complex for **3a** and **4a**. Given the values of the extinction coefficients falling in the 5000–8000 $dm^3\ mol^{-1}\ cm^{-1}$ range, these bands are too intense to be related to *d*-*d* transitions. The Vis spectrum of **5a**, instead, seems to result from a convolution of two different bands centered at λ_{max} = 440 nm and 490 nm (Figure 11).

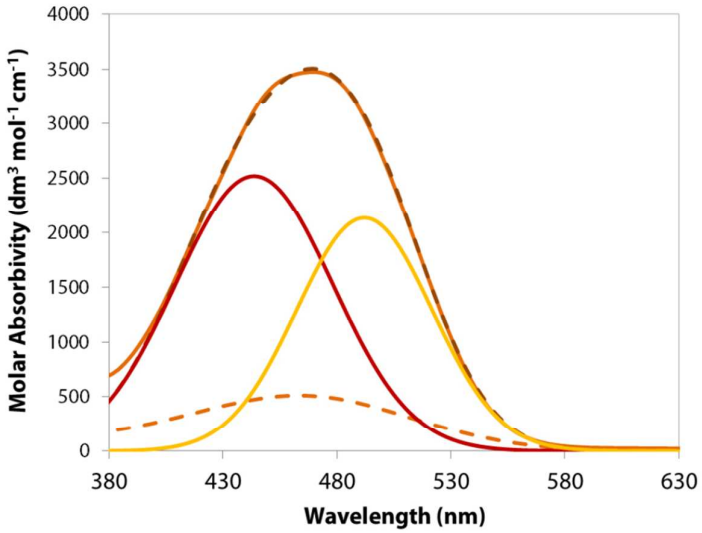

Figure 11. UV-Vis spectrum (380–630 nm) for **5a** (orange solid line) in CH_3CN solution superimposed with the calculated spectrum (brown dashed line) as sum of two deconvoluted absorption bands (red and yellow solid lines). The orange dashed line represents the UV-Vis spectrum of the free ligand **2** in the same solvent.

The presence of two bands in that region is further confirmed by the DR spectrum of **5a** in the crystalline state (Figure S13) where these bands are more resolved, red-shifted (λ_{max} = 425 and 515 nm) and broader than the one observed in solution, as a result of solid state effects.

The spectra of compounds **3b**-**5b** do not show any differences in comparison with what above described for compounds **3a**-**5a**, except for the contribution of the different counterion in the UV region.

TD-DFT calculations were also used on the closed-shell system $[Al(ClCNAn)_3]^{3-}$ in order to assign the Vis absorption band. The first five transitions computed with the TD-DFT are listed in Table S3. The calculation points to the presence of bands of small intensity around 500 nm. The bands with the highest oscillator strength (3 and 5, Table S3) are computed at 470 and 508 nm and each one originate from the main contribution of two

transitions with similar probability, involving the HOMO → LUMO+1 and HOMO-1 → LUMO (580 nm), and HOMO → LUMO+2 and HOMO-1 → LUMO+1 (470 nm) orbitals. These findings may provide a solid explanation to the above mentioned considerations made on the convolution of two main bands centered at 440 and 490 nm, giving rise to the broad absorption band observed in the experimental Vis region centered at ca. 470 nm. According to the calculated molecular orbitals, these transitions have Ligand-to-Ligand CT character without involvement of the metal. The MOs involved into the transitions are very similar to those of the free ligand. In fact, the HOMO-2, HOMO-1 and HOMO are π antibonding orbitals involving the C–CN and C–Cl moieties, whereas the LUMO, LUMO+1 and LUMO+2 are π antibonding orbitals involving the C=O groups (Figure 10).

A significantly different behaviour occurs for the open-shell systems $[Cr(ClCNAn)_3]^{3-}$ and $[Fe(ClCNAn)_3]^{3-}$. According to the quadruplet (S = 3/2) and sextet (S = 5/2) ground states for **3** and **4** respectively, a considerable number of transition can be expected. In order to properly model the absorption band, twenty and fifty transitions were computed for **3** and **4**, respectively. The calculated spectra consist of a complicated series of transitions in which more than one electron excitation contributes to a given optical absorption (Tables S4 and S5). For the Fe(III) complex the predicted number of bands in the Vis region is significantly higher with respect to the Cr(III) complex (Figure S14). Moreover, the visible band is well reproduced for the Cr(III) complex whereas for the Fe(III) complex, there are transitions with predicted moderate intensity occurring at approximately 760 nm (Table S5) that causes a considerable enlargement of the predicted band with respect to the experimental one (see Figure 10). An interesting feature that differentiate **3** and **4** with respect to **5** is that in the latter all the transition have Ligand-to-Ligand CT character, whereas in the formers most of the bands have Ligand-to-Metal CT character (Figure S15 and Tables S4 and S5). This may provide a route for the non-radiative decay responsible of the luminescence quenching of **3** and **4** (*vide infra*).

Photoluminescence Studies. The chlorocyananilate ligand shows emissive properties upon photoexcitation in the lowest absorption band, and the observed emission spectra of **1** and **2** are reported in Figure 12.

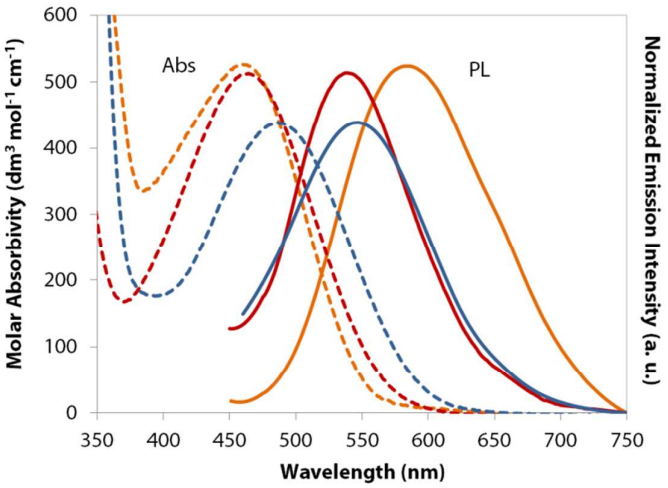

Figure 12. UV-Vis (dashed lines) and emission (solid lines) spectra (350–750 nm) for **2** in CH_3CN solution (orange line), and **1** in H_2O solution in its protonated (red line) and dianionic (blue line) forms.

The emission spectra of **1** were collected for the same solutions used for UV-Vis absorption measurements, under drastic acidic and basic conditions to ensure that the observed properties are related to the ligand in its protonated and dianionic forms, respectively. In both cases, when exciting in the lowest absorption band, emission in the green region, at ca. λ_{max} = 550 nm, is observed. Excitation spectra (Figure S16, Supporting Information) show a red-shift of the excitation maximum from 370 to 400 nm of the dianionic form of the chlorocyananilate ligand with respect to the acidic one, in accordance with the blue-shifted absorption spectrum of the protonated form when compared to the absorption band of the dianion in the same solvent. When a CH_3CN solution of **2** is irradiated at 400 nm, an emission band centered at ca. λ_{max} = 585 nm, related to the ligand in the dianionic form, is observed. Interestingly, on going from H_2O to CH_3CN a negative solvatochromism on varying the solvent polarity is observed for the emission band. Emission quantum yields (Φ) were estimated with the relative method (see Experimental Section) and their values for **1** in the dianionic and protonated forms, and **2**, are summarized in Table 4.

Table 4. Excitation (λ_{exc}) and emission (λ_{em}) wavelengths, and emission quantum yield values (Φ) for compounds **1** and **2**.

Compound	Solvent	λ_{exc} (nm)	λ_{em} (nm)	Φ (%)
1	H_2O (excess of HCl)	370	540	5.5(1)
	H_2O (excess of Et_3N)	400	550	5.5(1)

2	CH_3CN	400	585	1.4(1)

The comparable quantum yields values of **1** in the protonated and dianionic forms, suggest that the electrons located on oxygen atoms are not predominantly involved in the electronic transition responsible for the luminescent properties. This consideration is further supported by the fact that the position of the emission band of the protonated form is almost unchanged (λ_{max} = 540 nm) when compared to that of the dianion. It should be also pointed out that the lower value of the quantum yield for **2** is affected by a higher absorption value at the excitation wavelength. This can be related to the fact that the observed band may be considered as a convolution of the band of interest with an additional absorption band not leading to radiative states.

Whereas **3a** and **4a** are essentially non-emissive, likely due to the Ligand-to-Metal CT character of the electronic transition in the Vis region leading to non-radiative excited states (*vide supra*), the Al(III) complex **5a** still retains ligand-centered emission. Absorption and photoluminescence (PL) spectra in the Vis region of **5a** in CH_3CN solution are reported in Figure 13.

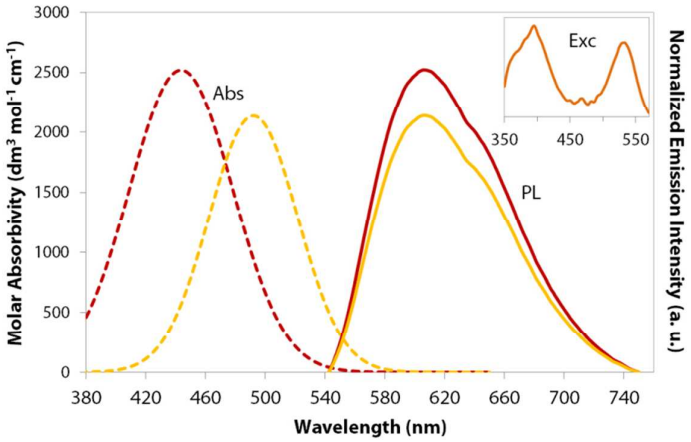

Figure 13. UV-Vis absorption (dashed lines), and continuous wave PL (solid lines) spectra (350–740 nm) for **5a** in CH_3CN solution. In the inset the excitation spectrum monitored at 605 nm is reported. Colour codes: red and yellow dashed lines = deconvoluted absorption bands, red solid line = PL upon irradiation at 390 nm, yellow solid line = PL upon irradiation at 530 nm. PL intensities were normalized for absorption at excitation wavelength.

Upon excitation in the Vis region, **5a** displays intense emission at λ_{max} = 605 nm. Interestingly, the related excitation spectrum, reported in the inset of Figure 13, consists of two main bands centered at 390 and 530 nm. This is in agreement with the previous considerations made for the absorption spectrum, *i.e.* that two different absorption bands are

convoluted into the experimental observed one (Figure 11). Emission quantum yields (Φ) for **5a** at the two excitation wavelengths values was estimated with the relative method (see Experimental Section) and the obtained values are reported in Table 5.

Table 5. Excitation (λ_{exc}) and emission (λ_{em}) wavelengths, and emission quantum yield values (Φ) for **5a**.

Compound	λ_{exc} (nm)	λ_{em} (nm)	Φ (%)
5a	390	605	1.2(1)
	530	605	0.8(1)

Interestingly, the maximum quantum yield is achieved when exciting on the higher energy side of the 380–540 nm absorption band (see Figure 13).

It can be concluded that coordination to Al(III), does not significantly affect the luminescence properties of the free ligand, inducing a slight red-shift in the emission wavelength while maintaining the same emission efficiency with comparable quantum yields. As far as the absorption and PL properties of compound **5b** are concerned, the same considerations made for **5a** are applied.

Magnetic measurements. The temperature dependence of the magnetic susceptibility for **3a** and **4a** are shown in Figure 14 as $\chi_m T$ versus T plots. The $\chi_m T$ values at room temperature, of ca. 1.9 $cm^3 K mol^{-1}$ and 4.4 $cm^3 K mol^{-1}$ for **3a** and **4a**, respectively, are close to the expected values (1.875 $cm^3 K mol^{-1}$ and 4.375 $cm^3 K mol^{-1}$) for isolated Cr(III) (S = 3/2, g = 2) and high spin Fe(III) (S = 5/2, g = 2) metal ions. These values remain constant in the whole temperature range, and only below 10 K the $\chi_m T$ products of both **3a** and **4a** show a slightly increase. The observed behaviors in the high temperature region (T > 10 K) are typical of magnetically isolated S = 3/2 (**3a**) or S = 5/2 (**4a**) ions, whereas the observed increases at low temperature are likely due to very weak magnetic interactions between the isotropic magnetic sites. On the basis of the crystal structures (*vide supra*) that highlight the presence of short Cl···N contacts between complex anions, the magnetic data have been modelled in the frame of the mean-field approximation using the Curie-Weiss law.

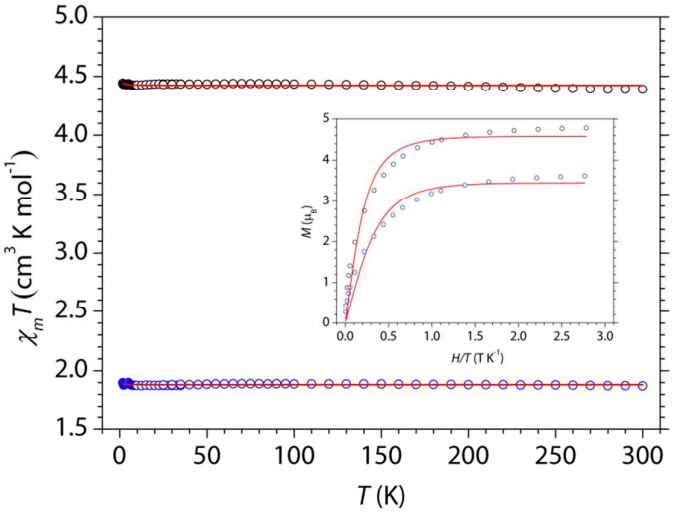

Figure 14. Temperature dependence of $\chi_m T$ between 1.80 and 300 K for polycrystalline samples of **3a** (blue circles) and **4a** (black circles). The solid red lines are the best fits obtained using the Curie-Weiss law. Inset: Field dependence of the magnetization for **3a** and **4a** (same colour codes) at 1.80 K, for magnetic fields between 0 and 5 T. The red solid lines are the best fits obtained using a $S = 3/2$ (**3a**) or $S = 5/2$ (**4a**) Brillouin function.

This model satisfactorily reproduces the magnetic properties of compounds **3a** and **4a** in the whole temperature range, with $g = 2.00(1)$ and $2.01(1)$, and $zJ/k_B = +11$ mK and +9 mK, for **3a** and **4a**, respectively. The magnitude of the inter-complex magnetic interactions, of the order of a few mK, falls well in the range expected for dipolar magnetic interactions but this observation does not rule out the possibility to have extremely small coupling also mediated by Cl···N interactions. The field dependence of the magnetization at 1.8 K supports the $S = 3/2$ and $S = 5/2$ ground spin state of the Cr(III) and Fe(III) ions since the corresponding Brillouin functions for $S = 3/2$ and $S = 5/2$ spin states, satisfactorily reproduce the experimental data with $g = 2.10(8)$, and 1.93(5) for **3a** and **4a**, respectively (Inset in Figure 14). Thus, **3a** exhibits Cr(III) ions with a $S = 3/2$ ground spin state, **4a** exhibits Fe(III) ions in high spin configuration with a $S = 5/2$ ground spin state, and both compounds show a typical paramagnetic behaviour of isolated ions.

The thermal variation of the magnetic susceptibility for **3b** and **4b** are shown in Figure 15 as $\chi_m T$ versus T plots. The $\chi_m T$ values at room temperature, of ca. 1.9 $cm^3\ K\ mol^{-1}$ and 4.4 $cm^3\ K\ mol^{-1}$, for **3b** and **4b**, respectively, are close to the expected values (1.875 $cm^3\ K\ mol^{-1}$ and 4.375 $cm^3\ K\ mol^{-1}$) for isolated Cr(III) ($S = 3/2$, $g = 2$) and high spin Fe(III) ($S = 5/2$, $g = 2$) metal ions. The $\chi_m T$ values remain constant down to ca. 20 K, then, $\chi_m T$ for **3b** shows a slightly increase to 2.2 $cm^3\ K\ mol^{-1}$ at 1.80 K, while for **4b** shows a slightly decrease to 4.1 $cm^3\ K\ mol^{-1}$ at 1.80 K. The observed behaviours in the high temperature region ($T > 20$ K) are

typical of magnetically isolated S = 3/2 (**3b**) or S = 5/2 (**4b**) ions, whereas the observed increase/decrease at low temperature are likely due to weak magnetic interactions between the isotropic magnetic sites. On the basis of the crystal structures (*vide supra*) that highlight the presence of quite isolated complex anions surrounded by $[Ph_4P]^+$ cations, the magnetic data have been modelled in the frame of the mean-field approximation using the Curie-Weiss law to evaluate the strength of these interactions.

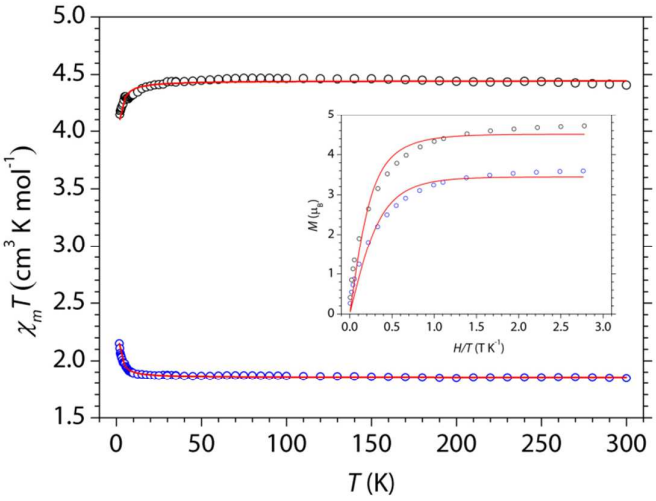

Figure 15. Temperature dependence of $\chi_m T$ between 1.80 and 300 K for polycrystalline samples of **3b** (blue circles) and **4b** (black circles). The solid red lines are the best fits obtained using the Curie-Weiss law. Inset: Field dependence of the magnetization for **3b** and **4b** (same colour codes) at 1.80 K for magnetic fields between 0 and 5 T. The red solid lines are the best fits obtained using a S = 3/2 (**3b**) or S = 5/2 (**4b**) Brillouin function.

This model satisfactorily reproduces the magnetic properties of compounds **3b** and **4b** in the whole temperature range, with g = 1.99(1) and 2.02(1), and zJ/k_B = +344 mK and –237 mK, for **3b** and **4b**, respectively. The magnitude of the inter-complex magnetic interactions of the order of mK falls well in the range expected for dipolar magnetic interactions, the only expected type of magnetic interactions for these compounds given the absence of direct intermolecular contacts between magnetic centers. Interestingly, the small magnetic interactions observed in compounds **3b** and **4b** show similar magnitude, in agreement with their isostructurality, but different sign, *i.e.* ferromagnetic in **3b** and antiferromagnetic in **4b**. The field dependence of the magnetization at 1.8 K supports the S = 3/2 and S = 5/2 ground spin state of the Cr(III) and Fe(III) ions since the corresponding Brillouin functions for S = 3/2 and S = 5/2 spin states satisfactorily reproduce the experimental data with g = 2.13(5) and 1.90(5), for **3b** and **4b**, respectively (Inset in Figure 15). Thus, **3b** exhibits Cr(III) ions with a S = 3/2 ground spin state, **4b** exhibits Fe(III) ions in high spin configuration with a S = 5/2

ground spin state, and both compounds show a typical paramagnetic behaviour of quasi-isolated ions.

CONCLUSIONS

The optimized synthesis and full characterization of the novel chlorocyananilate ligand ($ClCNAn^{2-}$), a unique example of a heterosubstituted multi-acting anilate tecton, bearing one chlorine atom and one cyano group, have been reported and its electronic, luminescent properties and coordination chemistry investigated. The synthesis and physical properties of its tris-chelated isostructural metal complexes with *d* (Cr(III), Fe(III)) and *p* (Al(III)) metal ions are also described, representing, in the family of anilate-based materials, the first examples containing an asymmetrically substituted anilate ligand where the substituent exchange strongly affects their chemical and physical properties. In particular, from the structural point of view, the peculiar ability of this multi-acting tecton to behave simultaneously as a halogen-bonding donor and acceptor, increases the number of supramolecular interactions exchanged by its metal complexes leading to an interesting molecular packing consisting of 1D supramolecular chains. In addition, its asymmetric structure has influence on the shape and energy distribution of the molecular orbitals involved into the electronic excitations. In particular, the HOMO → LUMO transition in the Vis region leads to an excited state associated to light emission properties unprecedentedly observed in the class of anilate-based materials. Furthermore, the Al(III) complex, $[Al(ClCNAn)_3]^{3-}$ is an appealing red luminophore under convenient visible light irradiation. The corresponding isostructural complexes with *d*-metal ions, namely $[Cr(ClCNAn)_3]^{3-}$ and $[Fe(ClCNAn)_3]^{3-}$ exhibit the typical paramagnetic behavior of this family of mononuclear complexes[11,22]. Therefore, while the rational design and synthesis of chlorocyananilate-based complexes with closed-shell trivalent metal ions such as Al(III) represent a promising molecular strategy and a powerful tool for introducing luminescence properties into multifunctional molecular materials, open-shell *d*-metal complexes are suitable to be employed as molecular building blocks for the preparation of molecule-based magnets[14] or organic/inorganic conducting/magnetic hybrid systems[18] It has to be pointed out that the isostructurality of all complexes allows for combination of molecular building blocks with different physical properties simply on changing the coordinated metal ion, without altering the topology and the supramolecular architecture of the desired functional molecular material.

As perspective, more detailed photophysical studies are in progress in order to check the chlorocyananilate ability to work as antenna ligand towards *4f*-metal ions, whose intense, sharp and long-lived emissions, make such potential lanthanide-based compounds particularly interesting for a variety of optical uses such as display devices and luminescent sensors or as excellent candidates for the construction of magnetic/luminescent molecular materials.

EXPERIMENTAL SECTION

Synthesis.

KHClCNAn (1). 2,3-dicyano-5,6-dichloro-1,4-benzoquinone (5 g, 0.022 mol) was suspended in H_2O (150 mL) and the mixture was stirred and heated at ca. 60 °C. A 6 M KOH aqueous solution (30 mL) was slowly added to the orange solution that became deep-red. After 30 min under stirring at 60 °C, the 2,3-dicyano-5,6-dichloro-1,4-benzoquinone was completely dissolved, and the solution was concentrated to half of the initial volume and kept at 4 °C overnight to favor the precipitation of the potassium salt of chlorocyananilate. The dark-red needle-like crystals were filtered and washed several time with a 3 M KOH aqueous solution, then with acetone, and air-dried. The potassium salt (3 g) was then dissolved in H_2O (100 mL) by heating, then the solution filtered and acidified with concentrate HCl. The deep-red solution was concentrated to ca. 50 mL by rota-evaporation, until the incipient precipitation of **1** as red-orange shiny crystals suitable for X-ray analysis. (yield 40%). Elemental analysis calcd. (%) for C_7HClNO_4K: C 37.95, H 0.45, N 6.32; found: C 37.58, H 0.39, N 6.25. ^{13}C NMR (125 MHz, D_2O): δ = 177.1, 169.0, 117.8, 112.5, 92.2, 86.5. FT-IR ($\bar{\upsilon}_{max}$/cm^{-1}, KBr pellets): 3462(w, broad), 3069(m, broad), 2236(vs), 2207(s), 1676(m), 1636(m), 1625(m), 1578(vs), 1400(m), 1361(w), 1300(m), 1271(m), 1184(m), 1004(m), 863(m), 801(m), 779(m), 752(w), 653(w), 607(m), 550(w), 479(w). ESI-MS, *m/z* found (calcd) = 197.75 (197.96) $[ClCNAn–H]^-$; UV-Vis (H_2O solution acidified with concentrated HCl, λ_{max}/nm (ε/dm^3 mol^{-1} cm^{-1})): 251 (10405), 305 (16036), 464 (512); UV-Vis (H_2O solution basified with NEt_3, λ_{max}/nm (ε/dm^3 mol^{-1} cm^{-1})): 261 (13361), 316 (19973), 487 (438).

$[Ph_4P]_2[ClCNAn]\cdot 2H_2O$ (2). **1** (50 mg, 0.20 mmol) was dissolved under heating in a H_2O solution (100 mL) containing NaOH (20 mg, 0.50 mmol) and Ph_4PBr (210 mg, 0.50 mmol). By cooling slowly the solution, **2** precipitates as orange shiny crystals suitable for X-ray analysis. Elemental analysis calcd. (%) for $C_{55}H_{44}ClNO_6P_2$: C 72.41, H 4.86, N 1.54; found:

C 72.35, H 4.73, N 1.59. FT-IR ($\bar{\upsilon}_{max}$/cm^{-1}, KBr pellets): 3479(m, broad), 3057(w), 2208(w), 2188(m), 1624(m), 1586(w), 1558(s), 1530(vs), 1484(m), 1435(s), 1376(w), 1340(w), 1314(w), 1196(w), 1109(s), 997(m), 827(w), 763(m), 725(s), 694(m), 609(m), 530(vs), 461(w). UV-Vis ($CHCN_3$ solution, λ_{max}/nm (ε/dm^3 mol^{-1} cm^{-1})): 268 (19718), 318 (23262), 460 (526). ESI-MS, *m/z* found (calcd) = 197.75 (197.96) [ClCNAn–H]$^-$; 535.88 (536.08) [[Ph_4P][ClCNAn]]$^-$.

[(*n*-Bu)$_4$N]$_3$[Cr(ClCNAn)$_3$] (3a). An aqueous solution (5 mL) of $CrCl_3 \cdot 6H_2O$ (61 mg, 0.22 mmol) was added dropwise to an aqueous solution (50 mL) of KHClCNAn (154 mg, 0.65 mmol), NaOH (26 mg, 0.66 mmol) and (*n*-Bu)$_4$NBr (213 mg, 0.66 mmol). After ca. 30 min of stirring at 60 °C, **3a** starts to precipitate as red-violet solid partially soluble in water. The mixture was allowed to cool to 25 °C, and the precipitate separated from the mother liquor by filtration. The filtrate was washed several times with fresh water and dried in desiccator under vacuum. Compound **3a** was crystallized in MeOH to give red shiny crystals suitable for X-ray analysis. Yield: 85%. Elemental anal. Calcd for $C_{69}H_{108}Cl_3CrN_6O_{12}$: C, 60.40; H, 7.93; N, 6.13; Found. C, 60.29; H, 7.92; N, 6.20. FT-IR ($\bar{\upsilon}_{max}$/cm^{-1}, KBr pellets): 2963(m), 2934(w), 2876(m), 2213(m), 1644(m), 1612(w), 1562(s), 1528(vs), 1480(m), 1395(vs), 1324(m), 1306(m), 1262(m), 1032(m), 882(w), 862(m), 740(w), 624(m), 610(m), 596(m), 517(w), 444(w). UV-Vis (CH_3CN solution, λ_{max}/nm (ε/dm^3 mol^{-1} cm^{-1})): 253 (39521), 323 (40932), 450 sh, 480 (6098). ESI-MS, *m/z* Found (Calcd) = 1429.30 (1429.52) [[(*n*-Bu)$_4$N]$_2$[Cr(ClCNAn)$_3$]]$^-$; 443.29 (443.53) [[(*n*-Bu)$_4$N][Cr(ClCN$_2$An)$_3$]]$^{2-}$.

[Ph$_4$P]$_3$[Cr(ClCNAn)$_3$]·H$_2$O (3b). This compound was synthesized as red shiny crystals according to the procedure described for **3a**, using $CrCl_3 \cdot 6H_2O$ (61 mg, 0.22 mmol), KHClCNAn (154 mg, 0.65 mmol), NaOH (26 mg, 0.66 mmol) and Ph_4PBr (277 mg, 0.66 mmol). Yield: 79%. Elemental anal. Calcd for $C_{93}H_{62}Cl_3CrP_3N_3O_{13}$: C, 66.46; H, 3.72; N, 2.50; Found. C, 66.02; H, 3.67; N, 2.47. FT-IR ($\bar{\upsilon}_{max}$/cm^{-1}, KBr pellets): 3063(w), 2211(s), 1636(m), 1610(w), 1560(s), 1526(vs), 1484(m), 1438(s), 1393(vs), 1306(m), 1263(m), 1188(w), 1165(w), 1108(s), 1031(m), 997(m), 863(m), 755(m), 724(s), 690(s), 625(m), 608(m), 595(m), 527(s), 443(w). UV-Vis (CH_3CN solution, λ_{max}/nm (ε/dm^3 mol^{-1} cm^{-1})): 253 (47504), 261 (46693), 275 (25544), 327 (45629), 450 sh, 479 (5615). ESI-MS, *m/z* Found (Calcd) = 1322.95 (1323.37) [[Ph_4P]$_2$[Cr(ClCNAn)$_3$]]$^-$; 982.84 (983.98) [[Ph_4P][Cr(ClCNAn)$_3$]–H]$^-$; 491.72 (491.99) [[Ph_4P][Cr(ClCNAn)$_3$]]$^{2-}$.

[(*n*-Bu)$_4$N]$_3$[Fe(ClCNAn)$_3$] (4a). This compound was synthesized as dark-red shiny crystals according to the procedure described for **3a**, using $FeCl_3$ (35 mg, 0.22 mmol), KHClCNAn (154 mg, 0.65 mmol), NaOH (26 mg, 0.66 mmol) and (*n*-Bu)$_4$NBr (213 mg, 0.66 mmol). Yield: 95%. Elemental anal. Calcd for $C_{69}H_{108}Cl_3FeN_6O_{12}$: C, 60.24; H, 7.91; N, 6.11; Found. C, 60.04; H, 7.90; N, 6.12. FT-IR ($\bar{\upsilon}_{max}$/cm^{-1}, KBr pellets): 2963(m), 2934(w), 2876(m), 2213(m), 1653(m), 1612(w), 1560(s), 1529(vs), 1480(m), 1395(vs), 1327(m), 1308(m), 1257(m), 1026(m), 883(w), 859(m), 740(w), 611(m), 577(m), 511(w), 418(w). UV-Vis (CH_3CN solution, λ_{max}/nm (ε/dm^3 mol^{-1} cm^{-1})): 254 (44032), 310 (34486), 354 (41694), 434 (6373), 465 (7572), 494 (7725). ESI-MS, *m/z* Found (Calcd) = 1133.27 (1133.37) [[(*n*-Bu)$_4$N]$_2$[Fe(ClCNAn)$_3$]]$^-$; 890.01 (890.90) [[(*n*-Bu)$_4$N][Fe(ClCNAn)$_3$]–H]$^-$; 445.34 (445.34) [[(*n*-Bu)$_4$N][Fe(ClCN$_2$An)$_3$]]$^{2-}$.

[Ph$_4$P]$_3$[Fe(ClCNAn)$_3$]·H$_2$O (4b). This compound was synthesized as red shiny crystals according to the procedure described for **3a**, using $FeCl_3$ (35 mg, 0.22 mmol), KHClCNAn (154 mg, 0.65 mmol), NaOH (26 mg, 0.66 mmol) and Ph_4PBr (277 mg, 0.66 mmol). Yield: 85%. Elemental anal. Calcd for $C_{93}H_{62}C_3FeP_3N_3O_{13}$: C, 66.31; H, 3.71; N, 2.49; Found. C, 65.76; H, 3.46; N, 2.50. FT-IR ($\bar{\upsilon}_{max}$/cm^{-1}, KBr pellets): 3063(w), 2211(s), 1636(m), 1610(w), 1560(s), 1526(vs), 1484(m), 1438(s), 1393(vs), 1306(m), 1263(m), 1188(w), 1165(w), 1108(s), 1026(m), 997(m), 860(m), 756(m), 724(s), 690(s), 610(m), 577(m), 528(s), 419(vw). UV-Vis (CH_3CN solution, λ_{max}/nm (ε/dm^3 mol^{-1} cm^{-1})): 250 (53308), 260 (52409), 275 (26494), 309 (36290), 355 (42171), 433 (7340), 463 (8310), 490 (8217). ESI-MS, m/z Found (Calcd) = 1326.92 (1327.22) [[Ph$_4$P]$_2$[Fe(ClCNAn)$_3$]]$^-$; 988.81 (988.83) [[Ph$_4$P][Fe(ClCNAn)$_3$]–H]$^-$; 493.67 (493.92) [[Ph$_4$P][Fe(ClCNAn)$_3$]]$^{2-}$.

[(*n*-Bu)$_4$N]$_3$[Al(ClCNAn)$_3$] (5a). This compound was synthesized as orange shiny crystals according to the procedure described for **3a**, using $Al_2(SO_4)_3 \cdot 18H_2O$ (73 mg, 0.11 mmol), KHClCNAn (154 mg, 0.65 mmol), NaOH (26 mg, 0.66 mmol) and (*n*-Bu)$_4$NBr (213 mg, 0.66 mmol). Yield: 94%. Elemental anal. Calcd for $C_{69}H_{108}Cl_3AlN_6O_{12}$: C, 61.53; H, 8.08; N, 6.24; Found. C, 61.07; H, 8.01; N, 6.14. FT-IR ($\bar{\upsilon}_{max}$/cm^{-1}, KBr pellets): 2963(m), 2934(w), 2876(m), 2214(m), 1649(m), 1613(w), 1583(s), 1550(vs), 1480(m), 1403(vs), 1336(m), 1313(m), 1265(m), 1036(m), 882(w), 865(m), 740(w), 636(m), 612(m), 598(m), 549(vw), 489(w), 450(w). UV-Vis (CH_3CN solution, λ_{max}/nm (ε/dm^3 mol^{-1} cm^{-1})): 249 (45041), 257 (40522), 323 (57591), 469 (3476). ESI-MS, *m/z* Found (Calcd) = 1588.85 (1589.42) [[(*n*-

$Bu)_4N]_4[Al(ClCNAn)_3]]^+$; 1102.29 (1104.50) $[[(n\text{-}Bu)_4N]_2[Al(ClCNAn)_3]]^-$; 430.78 (431.02) $[[(n\text{-}Bu)_4N][Al(ClCN_2An)_3]^{2-}$.

$[Ph_4P]_3[Al(ClCNAn)_3]\cdot H_2O$ (5b). This compound was synthesized as orange shiny crystals according to the procedure described for **3a**, using $Al_2(SO_4)_3\cdot 18H_2O$ (73 mg, 0.11 mmol), KHClCNAn (154 mg, 0.65 mmol), NaOH (26 mg, 0.66 mmol) and Ph_4PBr (277 mg, 0.66 mmol). Yield: 85%. Elemental anal. Calcd for $C_{93}H_{62}C_3AlP_3N_3O_{13}$: C, 67.46; H, 3.77; N, 2.54; Found. C, 66.59; H, 3.49; N, 2.44. FT-IR ($\bar{\upsilon}_{max}$/cm^{-1}, KBr pellets): 3063(w), 2212(s), 1647(m), 1610(w), 1583(s), 1548(vs), 1484(m), 1438(s), 1402(vs), 1355(m), 1314(m), 1263(m), 1188(w), 1165(w), 1108(s), 1031(m), 997(m), 866(m), 755(m), 724(s), 690(s), 637(m), 608(m), 595(m), 527(s), 490(vw), 450(vw). UV-Vis (CH_3CN solution, λ_{max}/nm (ε/dm^3 mol^{-1} cm^{-1})): 249 (49354), 257 (46909), 276 (20633), 314 (56351), 470 (3464). ESI-MS, m/z Found (Calcd) = 1976.02 (1977.14) $[[Ph_4P]_4[Al(ClCNAn)_3]]^+$; 1297.93 (1298.36) $[[Ph_4P]_2[Al(ClCNAn)_3]]^-$; 959.81 (959.97) $[[Ph_4P][Al(ClCNAn)_3]-H]^-$; 479.22 (479.49) $[[Ph_4P][Al(ClCNAn)_3]]^{2-}$.

Characterization. FT-IR spectra were performed on KBr pellets with a *Bruker Equinox 55* spectrophotometer. C, H, N analyses were performed with a *Thermo Electron Analyzer CHNS Flash 2000*. ESI-MS spectra were performed with a *Bruker Esquire 3000 Ionic Trap* (TOF analyzer) in negative and positive mode. UV-Vis absorption spectra (800–200 nm) were recorded in CH_3CN or H_2O on a *Varian Cary 5* spectrophotometer. NMR spectra were recorded on a *Bruker Avance DRX 300* spectrometer (300 MHz for ^{1}H, 75 MHz for ^{13}C). Chemical shifts are expressed in parts per million (ppm, δ), downfield from TMS as an external reference. The following abbreviations are used: singlet (s), doublet (d), triplet (t), quartet (q), doublet of doublets (dd).

Photoluminescence Spectroscopy. Continuous wave emission spectra (450–750 nm) were collected in CH_3CN or H_2O solutions with a *Horiba-Jobin Yvon Fluoromax-4* spectrofluorimeter using a direct current (DC) Xenon lamp. All spectra were spectrally corrected for detector response. Bandpass was set as 5 nm slit width for each measurement. Emission quantum yields (Φ) were evaluated using the relative method[41] by means of the following equation

$$\Phi = \Phi_R \frac{1-10^{-A_R}}{1-10^{-A}} \frac{I}{I_R} \frac{n^2}{{n_R}^2}$$

where A_R and A are the absorbances of the reference and the sample, respectively, at the excitation wavelength, I_R and I indicate the integrated emission signal of the reference and the sample, respectively, and n_R and n indicate the refractive index of the solvent for the reference and the sample, respectively. $[Ru(bpy)_3]Cl_2$ ($\Phi_R = 0.063$) was used as reference.

Single Crystal X-Ray Crystallography. Single crystal X-ray diffraction measurements were performed on a *Bruker Nonius Kappa CCD* diffractometer, using graphite-monochromated MoK_α radiation ($\lambda = 0.71073$ Å). The structures were solved by direct methods (SHELXS-97) and refined on F^2 with full-matrix least squares (SHELXL-97),[42] using the Wingx software package.[43] The non-H atoms were refined with anisotropic displacement parameters. In the crystal structure of compounds **2**, **3a**, **3b**, and **4a**, the cyano and chloro substituents were found disordered in two equivalent positions related to two possible orientations of the ligand along an ideal plane formed by the planar benzoquinone ring. These atoms were refined with mixed sites occupancy factors. The results of the refinements converge for all compounds to a ca. 50/50 probability (0.48/0.52, 0.49/0.51, 0.45/0.55, 0.49/0.51, for **2**, **3a**, **3b**, and **4a**, respectively) to find the chloro and cyano substituents in the two positions. This indicates the absence of a preferential orientation of the ligand in these crystal structures. Such disorder was not found in the crystal structure of **1**. In addition to the disorder related to the orientation of the ligands just described, in the crystal structure of **3b** one of the ligands was found globally disordered in two slightly displaced positions that were refined with isotropic thermal parameters and with site occupancy factors of 0.77/0.23. The same situation, with slightly different occupancy factors, was also observed in the isostructural compounds $[Ph_4P]_3[Fe(Cl_2An)_3]\cdot H_2O$ and $[Ph_4P]_3[Fe(Br_2An)_3]\cdot H_2O$ already reported.[22] The crystallization water molecule of **3b** was refined without the hydrogen atoms. Graphical material was prepared with Mercury CSD 3.3.[44] A summary of the crystallographic data and the structure refinement for compounds **1-4** is reported in Table 6. Crystallographic data for the structures have been deposited in the Cambridge Crystallographic Data Centre (see Supporting Information).

Table 6. Summary of X-ray crystallographic data for **1**, **2**, **3a**, **3b**, **4a**.

	1	**2**	**3a**	**3b**	**4a**
Empirical formula	$C_7HClKNO_4$	$C_{55}H_{44}ClNO_6P_2$	$C_{69}H_{108}Cl_3FeN_6O_{12}$	$C_{93}H_{60}Cl_3CrN_3P_3O_{13}$	$C_{69}H_{108}Cl_3FeN_6O_{12}$
Formula weight	237.64	912.30	1371.96	1678.70	1375.81
Crystal size, mm	0.6 × 0.09 × 0.03	0.50 × 0.30 × 0.10	0.60 × 0.12 × 0.07	0.32 × 0.28 × 0.10	0.80 × 0.60 × 0.10
Crystal system	Monoclinic	Triclinic	Monoclinic	Monoclinic	Monoclinic

Space group	$P2_1/a$	$P-1$	$P2_1/a$	$P2_1/n$	$P2_1/a$
a, Å	7.039(1)	9.9874(5)	20.219(2)	13.202(2)	20.167(1)
b, Å	17.051(3)	11.0867(11)	13.162(3)	18.819(5)	13.190(3)
c, Å	7.106(1)	12.2489(9)	29.914(5)	32.627(7)	29.964(7)
α, deg.	90	88.863(8)	90	90	90
β, deg.	102.389(15)	68.550(6)	108.729(10)	91.914(14)	108.603(11)
γ, deg.	90	66.460(7)	90	90	90
V, Å^3	833.0(2)	1144.6(1)	7539(2)	8101(3)	7554(2)
Z	4	1	4	4	4
T, K	293(2)	293(2)	150(2)	150(2)	150(2)
ρ (calc), Mg/m^3	1.895	1.324	1.209	1.376	1.210
μ, mm^{-1}	0.941	0.207	0.317	0.367	0.365
θ range, deg.	3.19–26.99	1.81– 28.79	1.88–24.10	1.25–26.50	1.88–24.50
GooF	1.063	1.022	1.076	1.057	1.027
$R1$	0.0447	0.0583	0.0907	0.0734	0.0699
$wR2$	0.1043	0.1327	0.2062	0.1784	0.1420

$R1 = \Sigma||F_o|-|F_c||/\Sigma|F_o|$, $wR2 = [\Sigma[w(F_o^2-F_c^2)^2]/\Sigma[w(F_o^2)^2]]^{½}$, $w = 1/[\sigma^2(F_o^2) + (aP)^2 + bP]$, where $P = [\max(F_o^2,0) + 2F_c^2]/3$.

Powder X-Ray Crystallography. Wide-Angle Powder X-Ray Diffraction (PXRD) patterns on polycrystalline samples were recorded on a *Panalytical Empyrean* diffractometer equipped with a graphite monochromator on the diffracted beam, and a X'Celerator linear detector. The scans were collected within the range 5–40° (2θ) using CuK_α radiation (λ = 1.540 Å). The simulated patterns were generated from the atomic coordinates of the single-crystal structure solutions using the Mercury CSD 3.3 program[44] (copyright CCDC, http://www.ccdc.cam.ac.uk/mercury/) using a FWHM (full width at half maximum) of 0.15 and a 2θ step of 0.05.

Computational Details. Density functional theory calculations were performed on the isolated ClCNAn^{2-} anion and on the [M(ClCNAn)$_3$]$^{3-}$ (M = Cr(III) (**3**), Fe(III) (**4**), Al(III) (**5**)) complexes. The geometry of the anion was optimized with the B3LYP hybrid density functional[44,46] and the 6-31+G(d) basis set.[47] The geometries of the metal complexes were optimized with the B3LYP density functional and the LANL2DZ basis set with Hay and Wadt effective core potential (ECP)[48,49] for Fe, Cr and halogen atoms and the 6-31G basis set for the C, N, O, and Cl atoms.[50,51] Single point calculations were performed on the complexes by using the B3LYP density functional and the LANL2TZ with Hay and Wadt ECP for the Fe and Cr metal ions,[52-54] whereas C, N, O, Cl and Al atoms were treated with the 6-311+G(d)

basis set.[55] Natural bond orbital analysis and natural atomic charges were obtained from the natural population analysis (NPA) performed with the NBO 3.1 program[55] incorporated in the Gaussian03 package. Spin density and electrostatic potential diagrams were generated with the Gabedit[57] and MOLDEN[58] programs. To address the solvation effects in acetonitrile, the polarizable continuum model (PCM)[69] was also applied using gas-phase optimized geometries. TD-DFT[60,61] PCM calculations in CH_3CN were performed to obtain the energies of the ten lowest singlet electronic transitions for the ligand and the Al(III) complex. Twenty and fifty transitions were computed for the Cr(III) and Fe(III) complexes, respectively, using the B3LYP density functional and the lanl2dz basis set on the metal ion and the 3-21G basis set on the remaining atoms.[62] SWizard[63] was used to analyzed the electronic transitions obtained from TD-DFT calculations. All the calculations were performed with the Gaussian 03 program suite.[64]

Magnetic measurements. Susceptibility measurements were performed in the temperature range 1.8–300 K with applied magnetic fields of 0.1–1 T on polycrystalline samples of compounds **3-4** with masses of 11.48, 6.73, 8.98, and 4.11 mg, for **3a**, **4a**, **3b**, and **4b**, respectively, by using a *Quantum Design MPMS-XL-5 SQUID* susceptometer. The isothermal magnetization measurements were performed on the same samples at 1.8 K with magnetic fields up to 5 T with the same equipment. Susceptibility data were corrected for the sample holders previously measured using the same conditions and for the diamagnetic contributions as deduced by using Pascal's constant tables.[65] PXRD measurements have been performed on the same polycrystalline samples that were measured in the SQUID. They show experimental patterns that correspond to the simulated X-Ray patterns obtained from the single crystal X-Ray structures, confirming that the solved structures are representative of the entire measured samples. PXRD data are reported in the Supporting Information (Figures S4–S6).

ASSOCIATED CONTENT

Supporting Information

X-ray crystallographic file in CIF format, additional Figures as mentioned in the text. Crystallographic data for the structures have been deposited in the Cambridge Crystallographic Data Centre, deposition numbers CCDC 1052898 (**1**), CCDC 1052897 (**2**), CCDC 1052896 (**3a**), CCDC 1052895 (**3b**), CCDC 1052894 (**4a**). These data can be obtained

free of charge from The Cambridge Crystallographic Data Centre via www.ccdc.cam.ac.uk/data_request/cif.

AUTHOR INFORMATION

Corresponding Author

*E-mail: luciano.marchio@unipr.it. Fax: (+39)0521905557. Tel: (+39)0521905419.

*E-mail: mercuri@unica.it. Fax: (+39)0706754486. Tel: (+39)0706754486.

ACKNOWLEDGMENTS

This work was supported in Italy by Regione Autonoma della Sardegna, L.R. 7-8-2007, Bando 2009, CRP-17453 Project "Nano Materiali Multifunzionali per Applicazioni nell'Elettronica Molecolare", Fondazione Banco di Sardegna and INSTM. The work in France was supported by the CNRS, the University of Angers and the National Agency for Research (ANR) (ANR Inter, ANR-12-IS07-0004-04, CREMM project).

REFERENCES

1. (a) M. L. Mercuri, P. Deplano, L. Pilia, A. Serpe and F. Artizzu, *Coord. Chem. Rev.*, 2010, **254**, 1419–1433. (b) M. L. Mercuri, P. Deplano, A. Serpe and F. Artizzu, *Chapter 7, In Handbook of Multifunctional Molecular Materials, Multifunctional Nanomaterials of interest in Molecular Electronics*; 219−280; Ouahab, L., Ed.; Pan Stanford Publishing: Singapore, 2013.
2. (a) F. Pop, P. Auban-Senzier, E. Canadell, G. L. J. A. Rikken and N. Avarvari, *Nat. Commun.* **2014**, *5*:3757. (b) F. Pop, P. Auban-Senzier, A. Frąckowiak, K. Ptaszyński, I. Olejniczak, J. D. Wallis, E. Canadell and N. Avarvari, *J. Am. Chem. Soc.*, 2013, **135**, 17176–17186. (c) F. Pop, M. Allain, P. Auban-Senzier, J. Martínez-Lillo, F. Lloret, M. Julve, E. Canadell and N. Avarvari, *Eur. J. Inorg. Chem.,* 2014, 3855–3862. (d) C. Provent and A. F. Williams, *The Chirality of Polynuclear Transition Metal Complexes, in Transition Metals in Supramolecular Chemistry*, ed. J.-P. Seauvage, John Wiley & Sons Ltd, 1999.
3. (a) G. Cucinotta, M. Perfetti, J. Luzon, M. Etienne, P.-E. Car, A. Caneschi, G. Calvez, K. Bernot and R. Sessoli, *Angew. Chem., Int. Ed.,* 2012, **51**, 1606; (b) M.-E. Boulon, G. Cucinotta, J. Luzon, C. Degl'Innocenti, M. Perfetti, K. Bernot, G. Calvez, A. Caneschi and R. Sessoli, *Angew. Chem., Int. Ed.*, 2013, **52**, 350–354.

4. (a) L. Bogani and W. Wernsdorfer, *Nat. Mater.,* 2008, **7**, 179–186; (b) R. Vincent, S. Klyatskaya, M. Ruben, W. Wernsdorfer and F. Balestro, *Nature*, 2012, **488**, 357–360; (c) M. Urdampilleta, S. Klyatskaya, J.-P. Cleuziou, M. Ruben and W. Wernsdorfer, *Nat. Mater.*, 2011, **10**, 502–586.
5. J.-P. Launay and M. Verdaguer, *Electrons in Molecules: From Basic Principles to Molecular Electronics*, Oxford University Press, UK, 2014.
6. J. W. Steed and J. L. Atwood, *Supramolecular Chemistry*, 2nd edn, John Wiley & Sons, 2009.
7. J. W. Steed, D. R. Turner and K. J. Wallace, *Core concepts in supramolecular chemistry and nanochemistry*, John Wiley & Sons, 2007.
8. D. Braga, L. Brammer and N. R. Champness, *CrystEngComm,* 2005, **7**, 1–19.
9. L. Brammer, *Chem. Soc. Rev.,* 2004, **33**, 476–489.
10. S. Kitagawa and S. Kawata, *Coord. Chem. Rev.,* 2002, **224**, 11−34.
11. M. Atzori, L. Marchiò, R. Clérac, A. Serpe, P. Deplano, N. Avarvari and M. L. Mercuri, *Cryst. Growth Des.,* 2014, 14, 5938–5948.
12. I. Imaz, G. Mouchaham, N. Roques, S. Brandès and J.-P. Sutter, *Inorg. Chem.,* 2013, **52**, 11237−11243.
13. G. Mouchaham, N. Roques, C. Duhayon, I. Imaz and J.-P. Sutter, *New J. Chem.,* 2013, **37**, 3476−3487.
14. M. Atzori, S. Benmansour, G. Mínguez Espallargas, M. Clemente-León, A. Abhervé, P. Gómez-Claramunt, E. Coronado, F. Artizzu, E. Sessini, P. Deplano, A. Serpe, M. L. Mercuri and C. J. Gómez García, *Inorg. Chem.,* 2013, **52**, 10031–10040.
15. B. F. Abrahams, M. J. Grannas, T. A. Hudson, S. A. Hughes, N. H. Pranoto and R. Robson, *Dalton Trans.,* 2011, **40**, 12242−12247.
16. B. F. Abrahams, T. A. Hudson, L. J. McCormick and R. Robson, *Cryst. Growth Des.,* 2011, **11**, 2717−2720.
17. T.-T. Luo, Y.-H. Liu, H.-L. Tsai, C.-C. Su, C.-H. Ueng and K.-L. Lu, *Eur. J. Inorg. Chem.,* 2004, 4253−4258.
18. (a) M. Atzori, F. Pop, P. Auban-Senzier, C. J. Gómez-García, E. Canadell, F. Artizzu, A. Serpe, P. Deplano, N. Avarvari and M. L. Mercuri, *Inorg. Chem.,* 2014, **53**, 7028–7039. (b) M. Atzori, F. Pop, P.Auban-Senzier, R. Clérac, E. Canadell, M. L. Mercuri, and N. Avarvari, *Inorg. Chem.,* 2015, **54**, 3643–3653.

19. K. S. Min, A. G. DiPasquale, J. A. Golen, A. L. Rheingold and J. S. Miller, *J. Am. Chem. Soc.*, 2007, **129**, 2360–2368.
20. F. A. Cotton, C. A. Murillo, D. Villagrán and R. Yu, *J. Am. Chem. Soc.*, 2006, **128**, 3281–3290.
21. F. Tinti, M. Verdaguer, O. Kahn and J. M. Savariault, *Inorg. Chem.*, 1987, **26**, 2380-2384.
22. M. Atzori, F. Artizzu, E. Sessini, L. Marchiò, D. Loche, A. Serpe, P. Deplano, G. Concas, F. Pop, N. Avarvari and M. L. Mercuri, *Dalton Trans.,* 2014, **43**, 7006–7019.
23. M. Atzori, F. Pop, T. Cauchy, M. L. Mercuri and N. Avarvari, *Org. Biomol. Chem.,* 2014, **12**, 8752–8763.
24. M. M. Richter, *Ber. d. deutsch. chem. Ges.,* 1911, **44**, 3469–3477.
25. R. E. Rehwoldt, B. L. Chasen and J. B. Li, *Anal. Chem.,* 1966, **8**, 1018–1019.
26. K. Wallenfels and K. Friedrich, *Chem. Ber.,* 1960, **93**, 3070–3082.
27. E. K. Andersen, *Acta Cryst.,* 1967, **22**, 188–191.
28. E. K. Andersen, *Acta Cryst.,* 1967, **22**, 191–196.
29. E. K. Andersen and I. G. K. Andersen, *Acta Cryst. B,* 1975, **31**, 384–387.
30. D. Semmingsen, *Acta Chem. Scand. B,* 1977, **31**, 11–14.
31. A. Klug, *Acta Cryst.,* 1965, **19**, 983–992.
32. E. K. Andersen, *Acta Cryst.,* 1967, **22**, 196–201.
33. E. K. Andersen, *Acta Cryst.,* 1967, **22**, 201–203.
34. K. Molčanov, I. Sabljic and B. Kojić-Prodić, *CrystEngComm,* 2011, **13**, 4211–4217.
35. K. Molčanov, B. Kojić-Prodić, *Acta Cryst. B,* 2012, **68**, 57–65.
36. K. Molčanov, B. Kojić-Prodić, D. Babic and J. Stare, *CrystEngComm,* 2013, **15**, 135–143.
37. K. Molčanov, B. Kojic-Prodic and A. Meden, *CrystEngComm,* 2009, **11**, 1407–1415.
38. C. J. Cramer, *Essentials of Computational Chemistry. Theories and Models*, 2nd ed., John Wiley & Sons, Chichester, UK, 2004.
39. P. Politzer, J. S. Murray and P. Lane, *Int. J. Quantum Chem.,* 2007, **107**, 3046–3052.
40. A. Pawlukojć, I. Natkaniec, J. Nowicka-Scheibe, E. Grech and L. Sobczyk, *Spectrochim. Acta, Part A,* 2003, **59**, 537–542.
41. A. M. Brouwer, *Pure Appl. Chem.*, 2011, **12**, 213–2228.
42. G. M. Sheldrick, *Programs for the Refinement of Crystal Structures*, University of Göttingen: Göttingen, Germany, 1996.

43. L. J. Farrugia, *J. Appl. Crystallogr.*, 1999, **32**, 837.
44. C. F. Macrae, P. R. Edgington, P. McCabe, E. Pidcock, G. P. Shields, R. Taylor, M. Towler and J. van de Streek, *J. Appl. Crystallogr.,* 2006, **39**, 453−457.
45. A. D. Becke, *Phys. Rev. A,* 1988, **38**, 3098−3100.
46. A. D. Becke, *J. Chem. Phys.*, 1993, **98**, 5648−5652.
47. M. M. Francl, W. J. Pietro, W. J. Hehre, J. S. Binkley, D. J. DeFrees, J. A. Pople and M. S. Gordon, *J. Chem. Phys.*, 1982, **77**, 3654−3665.
48. P. J. Hay and W. R. Wadt, *J. Chem. Phys.,* 1985, **82**, 299−310.
49. W. R. Wadt and P. J. Hay, *J. Chem. Phys.,* 1985, **82**, 284−298.
50. R. Ditchfield, W. J. Hehre and J. A. Pople, *J. Chem. Phys.*, 1971, **54**, 724−728.
51. V. A. Rassolov, M. A. Ratner, J. A. Pople, P. C. Redfern and L. A. Curtiss, *J. Comp. Chem.,* 2001, **22**, 976−984.
52. P. J. Hay and W. R. Wadt, *J. Chem. Phys.,* 1985, **82**, 270.
53. D. Feller, *J. Comp. Chem.,* 1996, **17**, 1571−1586.
54. K. L. Schuchardt, B. T. Didier, T. Elsethagen, L. Sun, V. Gurumoorthi, J. Chase, J. Li and T. L. Windus, *J. Chem. Inf. Model.,* 2007, **47**, 1045−1052.
55. J. A. Pople, *J. Chem. Phys.,* 1980, **72**, 650.
56. E. D .Glendening, A. E. Reed, J. E. Carpenter and F. Weinhold, NBO, version 3.1.
57. A. R. Allouche, *J. Comp. Chem.,* 2011, **32**, 174−182.
58. G. Schaftenaar and J. H. Noordik, *J. Comput.-Aided Mol. Design*, 2000, **14**, 123−134.
59. J. Tomasi, B. Mennucci and R. Cammi, *Chem. Rev.*, 2005, **105**, 2999−3093.
60. M. E. Casida, C. Jamorski, K. C. Casida and D. R. Salahub, *J. Chem. Phys.,* 1998, **108**, 4439−4449.
61. R. E. Stratmann, G. E. Scuseria and M. J. Frisch, *J. Chem. Phys.*, 1998, **109**, 8218−8224.
62. K. D. Dobbs and W. J. Hehre, *J. Comp. Chem.,* 1986, **7**, 359−378.
63. S. I. Gorelsky, SWizard program, revision 4.6, http://www.sg-chem.net/.
64. M. J. Frisch, G. W. Trucks, H. B. Schlegel, G. E. Scuseria, M. A. Robb, J. R. Cheeseman, Jr. J. A. Montgomery, T. Vreven, K. N. Kudin, J. C. Burant, J. M. Millam, S. S. Iyengar, J. Tomasi, V. Barone, B. Mennucci, M. Cossi, G. Scalmani, N. Rega, G. A. Petersson, H. Nakatsuji, M. Hada, M. Ehara, K. Toyota, R. Fukuda, J. Hasegawa, M. Ishida, T. Nakajima, Y. Honda, O. Kitao, H. Nakai, M. Klene, X. Li, J. E. Knox, H. P. Hratchian, J. B. Cross, V. Bakken, C. Adamo, J. Jaramillo, R. Gomperts, R. E. Stratmann, O. Yazyev, A. J. Austin, R. Cammi, C. Pomelli; J. W. Ochterski, P. Y. Ayala, K. Morokuma, G. A.

Voth, P. Salvador, J. J. Dannenberg, V. G. Zakrzewski, S. Dapprich,; A. D. Daniels, M. C. Strain, O. Farkas, D. K. Malick, A. D. Rabuck, K. Raghavachari, J. B. Foresman, J. V. Ortiz, Q. Cui, A. G. Baboul, S. Clifford, J. Cioslowski, B. B. Stefanov, G. Liu, A. Liashenko, P. Piskorz, I. Komaromi, R. L. Martin, D. J. Fox, T. Keith, M. A. Al-Laham, C. Y. Peng, A. Nanayakkara, M. Challacombe, P. M. W. Gill, B. Johnson, W. Chen, M. W. Wong, C. Gonzalez and J. A. Pople, Gaussian 03, Revision C.02, *Gaussian, Inc.,* Wallingford CT, 2004.

65. R. L. Carlin, *Magnetochemistry*, 1986, Berlin, Springer.